



3D printing customised stiffness-matched meta-biomaterial with near-zero auxeticity for load-bearing tissue repair

Chameekara T. Wanniarachchi^a, Arun Arjunan^{a,*}, Ahmad Baroutaji^b, Manpreet Singh^a

^a Additive Manufacturing of Functional Materials (AMFM) Group, Centre for Engineering Innovation and Research, University of Wolverhampton, Telford Innovation Campus, Telford, TF2 9NT, United Kingdom

^b School of Engineering and Applied Science, Aston University, Aston Triangle, Birmingham, B4 7ET, United Kingdom

ARTICLE INFO

Keywords:

Laser powder bed fusion
3D printing
Metamaterials
Meta-biomaterials
Auxetic bone scaffold

ABSTRACT

The evolution of meta-biomaterials has opened up exciting new opportunities for mass personalisation of biomedical devices. This research paper details the development of a CoCrMo meta-biomaterial structure that facilitates personalised stiffness-matching while also exhibiting near-zero auxeticity. Using laser powder bed fusion, the porous architecture of the meta-biomaterial was characterised, showing potential for near-zero Poisson's ratio. The study also introduces a novel surrogate model that can predict the porosity (φ), yield strength (σ_y), elastic modulus (E), and negative Poisson's ratio ($-v$) of the meta-biomaterial, which was achieved through prototype testing and numerical modelling. The model was then used to inform a multi-criteria desirability objective, revealing an optimum near-zero $-v$ of -0.037 , with a targeted stiffness of 17.21 GPa. Parametric analysis of the meta-biomaterial showed that it exhibited $-v$, φ , σ_y and E values ranging from -0.02 to -0.08 , 73.63 – 81.38% , 41 – 64 MPa, and 9.46 – 20.6 GPa, respectively. In this study, a surrogate model was developed for the purpose of generating personalised scenarios for the production of bone scaffolds. By utilising this model, it was possible to achieve near-zero $-v$ and targeted stiffness personalisation. This breakthrough has significant implications for the field of bone tissue engineering and could pave the way for improved patient outcomes. The presented methodology is a powerful tool for the development of biomaterials and biomedical devices that can be 3D printed on demand for load-bearing tissue reconstruction. It has the potential to facilitate the creation of highly tailored and effective treatments for various conditions and injuries, ultimately enhancing patient outcomes.

1. Introduction

Meta-biomaterials, with their carefully designed porous architecture, can provide a unique combination of mechanical properties. These meta-biomaterials can be functionally designed to create personalised tissue engineering scaffolds [1–3]. One notable feature of auxetic meta-biomaterials is their negative Poisson's ratio, which means that the material expands laterally when stretched axially and contracts when compressed [4]. This behaviour offers distinct strain, deformation modes, and mechanical properties that differ from traditional biomaterials [5,6]. Recent studies suggest that auxetic behaviour, where applicable, can lead to superior scaffold-tissue interaction in the reconstruction of critical-size bone defects [7–9]. An ideal load-bearing scaffold should have mechanical properties, such as stiffness and strain

ratios, that compliments the host tissue being reconstructed [10,11].

When it comes to cellular materials, altering the pore size changes the structural behaviour such as the strength, stiffness, surface area and relative density [12–15]. However, this generally does not change the elastic strain behaviour influencing Poisson's ratio. Recent evidence [16–18] suggests that conventional strain behaviour in traditional biomaterials offer suboptimal stimulus required for tissue growth. Therefore, it is often necessary to modulate the mechanical properties of scaffolds for targeted strain behaviour and therefore the Poisson's ratio [19–22]. Developing meta-biomaterial scaffolds featuring targeted auxeticity ($-v$) and elastic modulus (stiffness) is a promising way to mimic the strain behaviour of host tissues in certain scenarios [23–25]. However, as put forward by Zadpoor [26,27], the main application of auxetic meta-biomaterials, comes down to the rational design of the

* Corresponding author. Additive Manufacturing of Functional Materials (AMFM) Group, Centre for Engineering Innovation and Research, University of Wolverhampton, Telford Innovation Campus, Telford, TF2 9NT, United Kingdom.

E-mail addresses: arun9624@gmail.com, a.arjunan@wlv.ac.uk (A. Arjunan).

<https://doi.org/10.1016/j.bprint.2023.e00292>

Received 6 April 2023; Received in revised form 30 May 2023; Accepted 15 June 2023

Available online 19 June 2023

2405-8866/© 2023 The Authors. Published by Elsevier B.V. This is an open access article under the CC BY license (<http://creativecommons.org/licenses/by/4.0/>).

geometry and mechanical properties in such a way as to optimise bone-scaffold interaction.

Meta-biomaterials are a subclass of metamaterials that possess distinct mechanical, physical, and biological properties that arise from their unique geometrical architecture [28,29]. The mechanical characteristics of these biomaterials are closely linked to their topological design and material composition [30]. Initially focused on orthopaedic applications, meta-biomaterials aim to enhance implant-bone tissue regeneration and mitigate the risk of implant-related infections [31]. Stress shielding, a phenomenon characterised by reduced stress on the bone due to the implant and micro-motions, poses a significant challenge at the bone-implant interface. However, the utilization of mechanical 3D meta-biomaterials offers a viable solution to address the mechanical mismatch between implants and bones [32]. Recent advancements in additive manufacturing (AM) have unlocked new possibilities for developing biomaterials and medical devices with unprecedented combinations of desirable properties and advanced functionalities. Surface bio-functionalisation techniques, infection prevention strategies, biodegradable metallic biomaterials, and composite biomaterials have all contributed to these advancements [25,33]. Consequently, meta-biomaterials show great potential as a cutting-edge approach for the development of long-term implants [34,35].

Studies that validate the influence of auxetic behaviour in yielding high proliferation and tissue reintegration are increasing [36–38]. Looking specifically at near-zero auxetic architecture [39–41] data to suggest that they offer improved stress and strain response to the host tissue favorable for wound healing. In other words, near zero $-v$ scaffolds may be beneficial to improve the overall healing process while offering a stimulating environment for tissue ingrowth. Research [42] on Polyethylene glycol (PEG) scaffolds, featuring near zero auxetic behaviour suggests they are also beneficial for engineering cartilage, corneal and ligament tissues. Kolken et al. [43] and Ghavidelnia et al. [32] examined cellular materials that offer a range of Poisson's ratio values as a result of their re-entrant unit cells. Numerical and experimental results confirmed that these architectures offer improved mechanical response under compressive loading. Although all these material architectures offered strain distribution suitable for tissue growth, $-v$ was found to offer enhanced tissue reintegration at the bone-implant interface [5,44,45].

Designing meta-biomaterials suitable for critical-size tissue reintegration also requires optimum porosity and mechanical property requirements [46–48]. Meta-biomaterials with sub-optimal mechanical properties cannot offer sufficient load-bearing support, particularly in bone tissue engineering [49–52]. On the contrary, relying on excessively stiff architecture hinders tissue reintegration because of stress shielding [53–55] and maladapted stress concentration [56,57]. This is where additive manufacturing (3D printing) technologies offer enormous potential due to their capacity for personalised on-demand fabrication [58, 59]. The use of AM to fabricate porous scaffold biomaterials have been investigated extensively to offer mass personalisation when the research matures [5,44,60].

Additive manufacturing (AM) offers a viable fabrication route for porous meta-biomaterials, subsequently informing its mechanical and biological behaviour [61–66]. As such the fundamental question when conceiving an auxetic meta-biomaterials becomes, what properties should be targeted when conceiving a near zero auxetic meta-biomaterials? Considering the challenges with stress-shielding and maladapted stress concentration dictated by the stiffness mismatch between implants and host bone [67–70]. Targeting stiffness (elastic modulus) to match the host section is a good starting point. In this regard, this research conceives a near-zero auxetic meta-biomaterial that is optimised to achieve a targeted stiffness of around 18 GPa of an adult tibial critical size section. This is done in a way that preserves other important parameters suitable for bone scaffolds such as porosity and strength [71–73].

Designer biomaterials [74–77] have been on the rise, but there is still

a lack of auxetic architectures that offer near-zero Poisson's ratio while also providing targeted stiffness matching. This research presents an open framework for the LPBF of near-zero auxetic meta-biomaterial scaffolds for tibial reconstruction. The use of CoCrMo as the bulk material allows for high porosity while preserving load bearing ability, critical for functional bone scaffolds. The scaffold's design parameters are algorithmically modified to achieve specific $-v$, stiffness, strength and relative density using a validated surrogate model. The generated scaffolds offer near-zero auxeticity while providing stiffness matching for user-defined scenarios. The framework presented can be used to refine and generate alternate prototypes of meta-biomaterials suitable for tissue reconstruction where near-zero auxeticity is advantageous.

2. Methodology

2.1. Conception of the meta-biomaterial architecture

2.1.1. Near-zero auxeticity

When it comes to developing auxetic materials, using a re-entrant architecture is one of the most efficient ways to achieve negative Poisson's ratio ($-v$). This is achieved through strategically assembling re-entrant unit cells to achieve lateral shrinkage under axial compression or vice versa [78,79]. When it comes to re-entrant unit cells, the chevron or the bowtie architecture is well known for offering high $-v$ [80,81]. From meta-biomaterial perspective, studies on bowtie auxetic architecture conducted by Kolken et al. [43,82] have confirmed high $-v$. On the contrary performance of auxetic variant that may be suitable for a near-zero Poisson's ratio such as the double-arrowhead architectures are yet to be studied from a load-bearing meta-biomaterial perspective.

A CoCrMo bone scaffold with a stiffness-matched near-zero Poisson's ratio was developed through the design of a double-arrowhead unit cell, inspired by the principles of polygon tessellation, as shown in Fig. 1. The unit cells were assembled to create interconnected porosity suitable for load-bearing bone scaffolds, while reducing overhangs to ensure selective laser melting without support structures. The unit cell was designed to fit a 2 mm cuboid, with variable parameters for strut thickness (t_s) and strut angle (θ_s) in the range of 0.38–0.48 mm and 15–25°, respectively, as shown in Fig. 1a. The meta-biomaterial scaffold was conceived by arranging the unit cells repeatedly in x, y, and z, as shown in Fig. 1b. This dimension was selected to reconstruct an 18 mm adult tibial critical-size bone defect (CSBD), which is a commonly encountered bone defect in clinical practice [83–85].

2.1.2. Additive manufacturing and surface morphology

The additive manufacturing of the meta-biomaterial specimens was performed using an EOS M290 3D printer. The composition of the CoCrMo feedstock used for the laser powder bed fusion featured 60–65% Co, 26–30% Cr and 5–7% Mo and trace elements of Si, Mn, Fe, C and Ni. The feedstock had a density of 8300 kg/m³ and a spherical morphology, making it suitable for LPBF, as depicted in Fig. 2. Although some deformed particles were occasionally present, they were not prevalent and were representative of high-quality commercial feedstock appropriate for LPBF. In general, the feedstock had a spherical shape, and its particle size ranged from 5 to 85 μ m, providing a high packing density.

Fabrication of all material samples was carried out using a constant laser power, hatch spacing, laser scanning speed, and layer depth of 290 W, 0.11 mm, 950 mm/s, and 40 μ m, respectively. The processing chamber maintained an inert argon environment with <0.1% oxygen, and three scaffold samples were fabricated under identical conditions for mechanical testing. Following the LPBF process, all the samples underwent an argon-filled heat-treated cycle of 1150 °C for 6 h. The test samples were then extracted from the build platform using a submerged wire electro-discharge machine (EDM) and characterised for strut thickness and surface quality using the EVO50 scanning electron microscopy (SEM).

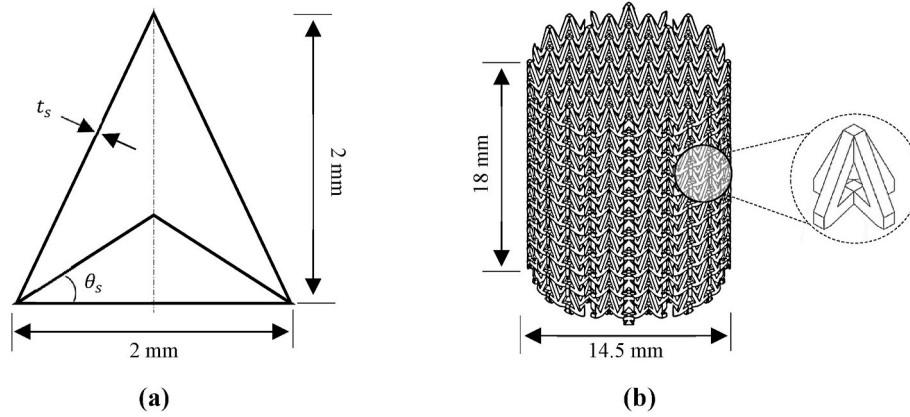


Fig. 1. Design evolution of the double-arrowhead auxetic meta-biomaterial showing (a) the unit-cell dimensions along with the variable parameters strut thickness (t_s) and strut angle (θ_s), and (b) the resulting meta-biomaterial bone scaffold with dimensions suitable to reconstruct a critical-size tibial defect.

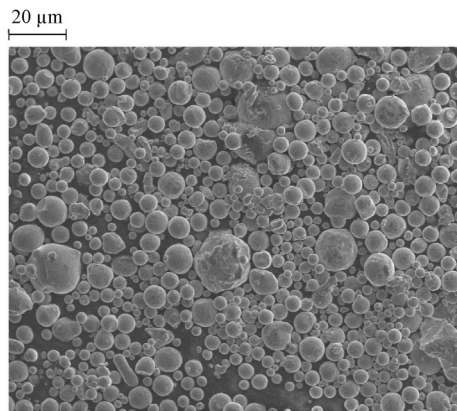


Fig. 2. SEM-informed morphology of the CoCrMo powder used for laser powder bed fusion.

2.1.3. Considerations for strut thickness

Additive manufacturing techniques, have certain constraints on the minimum achievable strut thickness. These constraints are primarily determined by the resolution capabilities of the specific technology and the properties of the materials used. In general, the minimum strut thickness that can be achieved through AM depends on factors such as the resolution of the printing system, the nozzle or laser diameter, the layer height, and the material's flow properties. Each additive manufacturing process has its own set of limitations and recommended design guidelines. It is essential to consider these limitations when designing and fabricating structures with AM techniques. Struts that are below the minimum achievable thickness may result in reduced structural integrity, poor surface finish, or difficulty in printing and post-processing. Therefore, it is necessary to understand the capabilities and limitations of the specific AM process being used and design the strut thickness accordingly within the achievable range. It is also worth noting that the desired mechanical properties and intended application of the structure may also impact the minimum strut thickness. Thinner struts may exhibit different mechanical behaviour, such as increased flexibility or reduced load-bearing capacity. Therefore, the design process should involve a careful consideration of both the AM process capabilities and the functional requirements of the structure to ensure an optimal balance between strut thickness and performance. For the L-PBF technology being employed in this study, the minimum achievable strut thickness is 80 μm [86,87], however considering structural integrity requirements for biomedical applications and repeatability a $>300 \mu\text{m}$ is recommended.

2.2. Surrogate modelling of the meta-biomaterial

2.2.1. Development of the parametric model

To develop an optimal near-zero Poisson's ratio meta-biomaterial scaffold, it is necessary to establish the relationship between the design parameters (t_s and θ_s) and critical responses of interest, such as porosity (φ), Poisson's ratio ($-v$), yield strength (σ_y), and elastic modulus (E). Therefore, a surrogate model is needed to establish the relationship between meta-biomaterial performance (φ , $-v$, σ_y , and E) and design variables (t_s and θ_s). Since there is no universal bone scaffold that can be used for all patients, the development of an optimised near-zero Poisson's ratio meta-biomaterial scaffold is crucial for successful bone regeneration.

The surrogate model was developed using a combination of numerical and statistical methods to establish the relationship between design parameters (t_s and θ_s) and performance measures of interest, (φ , $-v$, σ_y , and E) of the near-zero Poisson's ratio meta-biomaterial scaffold. The central composite design (CCD) response surface (RS) methodology informed the training matrix for the surrogate model, as it is a high-efficiency sampling approach that leads to accurate response surface models with fewer experiments. The steps taken to develop the surrogate model are summarised in Fig. 3. The relationship between resulting properties (y) and design changes (x) can be expressed using Eq. (1):

$$y = f(x_1, x_2, \dots, x_n) + \epsilon \quad (1)$$

where n and ϵ represents the variables and error connected to response y . Under such circumstances the 2nd order RS model can be written using Eq. (2):

$$y = \beta_0 + \sum_{i=1}^k \beta_i x_i + \sum_{i=1}^k \beta_{ii} x_i^2 + \sum_{i \neq j} \beta_{ij} x_i x_j + \epsilon \quad (2)$$

In the analysis of a randomized training matrix, the regression coefficients ($\beta_0, \beta_i, \beta_{ij}$ and β_{ii}) are used to describe the relationship between predictor variables and the response. These beta values are then utilised in the RS model to predict the values of x that correspond to a particular response. By performing parametric analysis, it is possible to determine the specific influences of t_s and θ_s on v , φ , σ_y and E . Once the parametric analysis is complete, the RS model can be used to optimise the meta-biomaterial architecture to meet a chosen multi-objective response criterion.

RS models are commonly used in cases where the number of input parameters affects the quality or performance of a design [88,89]. In the context of the meta-biomaterial scaffold under examination, t_s and θ_s are the parametric variables of interest for their impact on both $-v$ and the scaffold's other mechanical performances. Table 1 outlines how these variables correspond to the scaffold unit cell, with t_s chosen to achieve a

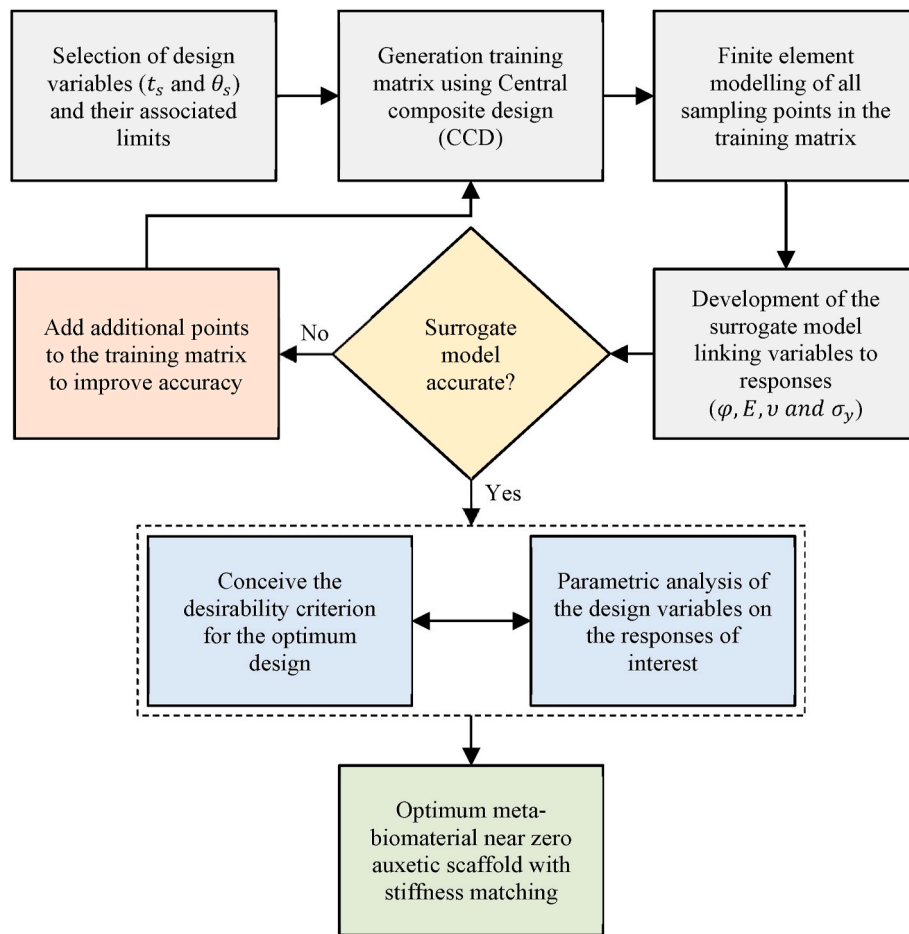



Fig. 3. Flow chart showing the methodology to conceive the surrogate model and to generate the optimum meta-biomaterial near-zero auxetic scaffold with the most desirable properties.

Table 1
Meta-biomaterial design variables are used to inform the surrogate model training matrix.

	Limits	Variables	
		θ_s (deg.)	t_s (mm)
	Min.	15	0.38
	Med.	20	0.43
	Max.	25	0.48

balance between porosity and its ability to deform under load. θ_s ranges from 15° to 25°, with the upper limit representing the highest feasible angle that does not penetrate the struts. The lower limit is set at 15° to prevent non-auxetic behaviour under compressive loading.

2.2.2. Formulation of the personalised stiffness-matched meta-biomaterial

The optimisation problem is formulated based on the response surface, which enables the identification of an ideal solution that satisfies the desired criteria. The criteria can be established by incorporating multiple objectives related to the design variables and parametric responses [80,90,91] as shown in Eq. (3):

$$\begin{cases} \text{Minimise } f(x) = [f_1(x), f_2(x), \dots, f_i(x)] \\ \text{s.t. } x^l \leq x \leq x^u \end{cases} \quad (3)$$

where x^l represents the lower limits and x^u represents the upper limits of the variables parameters linked to the objective function $f(x)$ [92]. In order to design an optimal, near zero auxetic, stiffness matched

meta-biomaterial scaffold, it is necessary to obtain the desired responses as summarised in Table 2. These are the design parameters necessary to achieve lowest lateral strain and near-zero ν , highest strength, and targeted elastic modulus of 18 GPa [56] that matches cortical bone while maintaining high porosity.

2.3. Finite element modelling

2.3.1. Material model and boundary conditions

A validated finite element (FE) model was utilised to characterise the non-linear behaviour of all meta-biomaterial scaffolds informed by the surrogate model. The most appropriate material representation for this study was found to be the bilinear isotropic strain hardening (BISO) option. This assumes the material as featuring a linear region with its slope signified by the E_{blk} . The post-linear region start at σ_{blk} and continues to be perfectly plastic. All the material parameters informing the

Table 2
Multi-objective optimisation criteria to generate the near-zero meta-biomaterial bone scaffold.

Parameters of interest	Desirability criterion	Explanation
Negative Poisson's ratio (ν)	Near zero	Lowest elastic strain
Elastic modulus (E)	18 GPa	Targeted stiffness matching
Yield strength (σ_y)	Maximise	High strength
Porosity (φ)	Maximise	High porosity

numerical model is summarised in Table 3. These were experimentally derived from CoCrMo test specimens fabricated under the same conditions as the meta-biomaterials.

The finite element modelling was carried out using ANSYS 2021/R1 Static Structural Module employing the Mechanical Ansys Parametric Design Language (APDL) Solver. A ten-node higher-order tetrahedral element (SOLID187) was used for the analysis after examining numerous element types. The SOLID187 element is well-suited for irregular volumetric geometries, such as porous materials, due to its ability to deform in a quadratic manner, resulting in improved accuracy [93,94]. Additionally, it is superior to four-node tetrahedron elements in stress computations. This element comprises ten nodal components, each offering three degrees of freedom (DOF), translational in x , y , and z (Fig. 4a). The global boundary conditions applied are shown in Fig. 4b, with loading conditions modelled similarly to the experimental test case. Since the deformation of the end plates is not of interest, they are modelled as rigid bodies with frictional contact with the scaffold. To accurately capture the force-displacement relationship, the loading was conducted using 100 sub-steps. The lower platens were constrained in all directions, while the upper platens were displaced axially 10%. The frictional contact between the scaffold and the end plates was modelled with a coefficient of 0.1 for a more realistic simulation.

2.3.2. Model discretisation

The accuracy of FE models heavily depends on the quality of the discretisation (mesh) used. Typically, a finer mesh yields more precise results as it can better capture stress gradients across the element [95]. Stress-raisers such as fillets and sharp corners require a smaller element size to accurately predict elastic-plastic behaviour [96]. However, increasing element density exponentially increases solution time and generates large data. Thus, an optimal mesh should balance element density and solution time to create an efficient numerical model.

The convergence study was based on the force-displacement curve using a range of element length featuring a ten-node tetrahedral element. Fig. 5 illustrates that the mesh sensitivity is extremely low along the elastic range of the meta-biomaterial scaffold below a 0.1 mm element size. Thus, a mesh size of 0.1 mm is sufficient to predict both the E and σ_y of the scaffolds. This resulted in 1,488,321 elements and 2,862,589 nodes, requiring a solution time of 3579.2 s. The models were solved in a simulation high performance computer (HPC) assisted by 56 2.7 GHz cores, 1 TB RAM and 2 GV100 accelerators.

2.3.3. Poisson's ratio extraction

Poisson's ratio (ν) typically manifests as a positive value, indicating a tendency towards expansion in the lateral direction when subjected to compression. In mathematical terms, this is represented by the negative proportion of lateral strain to axial strain, as written in Eq. (4). Auxetic materials exhibit a converse response, resulting in a $-\nu$. For instance, when a cylindrical auxetic material undergoes axial compression, it experiences a contraction in the radial direction and a diminution of its transverse dimensions. The scaffold's deformation in the radial direction is affected by the strain along the lateral direction (ϵ_{lat}), as illustrated in Eq. (5). Strain data for the scaffold's six individual lattice layers were scrutinized separately, and the overall shrinkage was determined by

averaging these values. The $-\nu$ was then calculated through the traditional formula, which entails dividing the average lateral strain by the axial strain, ϵ_y , in this instance.

$$\nu_{yx} = - \left(\frac{\epsilon_{lat}}{\epsilon_y} \right) \quad (4)$$

$$\epsilon_{lat} = - \left(\frac{\epsilon_x + \epsilon_z}{2} \right) \quad (5)$$

2.4. Prototype testing

Physical tests were carried out on the printed meta-biomaterial scaffolds to reveal their stress-strain relationship and to validate the numerical model. The physical tests were performed on Zwick 1474 compressive testing machine calibrated to BSEN ISO 7500-1 standards [97]. The test rig is shown in Fig. 6 featuring a high-definition camera to capture the crush behaviour of the scaffold. Compression of the specimens ($n = 3$) was carried out to 50% of the height at a speed of 80 $\mu\text{m/s}$. The $\sigma - \epsilon$ behaviour for all the meta-biomaterial specimens was recorded and the yield strength was identified using the 0.2% offset method from the $\sigma - \epsilon$ curves and the $-\nu$ was computed from the transverse strain computed at each scaffold layer [80].

3. Results and discussion

3.1. Meta-biomaterial prototypes

Fig. 7a shows the prototypes on the build plate which were extracted using submerged wire EDM and shotblasted to remove disengaged particles uncovering a comparatively unblemished surface as shown in Fig. 7b. All the fabricated scaffolds preserved their open porosity without any feedstock contaminants and offered a range of pore sizes informed by their digital design. The varying pore sizes when compatible, generally enhance vascularisation, resulting in increased tissue reintegration [98]. A range of pore sizes is critical for bone scaffolds; while soft tissue regeneration usually starts with the smallest pores available, the larger channels offer the required permeability required for bone growth. Overall, a higher than 50% porosity informed by pore diameters 50–650 μm is the minimum requirement for segmental bone reconstruction scaffolds [99,100].

The porosity of the printed meta-biomaterial scaffolds developed in this study is summarised in Table 4. The printed meta-biomaterial architecture measured 81.98% porosity which is 5.64% lower than the design porosity of 86.74%. The reason for this is evident from the SEM data of the printed scaffold shown in Fig. 7b. Although shot blasting managed to remove a large proportion of the partially sintered feedstock adhering to the surfaces, they were still observed at narrow joints which contributed slightly to reduce the porosity. Generally, this effect only contributes to <1% difference in non-porous architectures, however, the large number of joints informing the meta-biomaterial architecture increased this discrepancy to 5.64% which was also observed by Tan et al. [101]. SEM data also revealed a variation in the strut thickness of the fabricated scaffolds averaging to $\sim 29 \mu\text{m}$ which was also observed in other materials using LPBF [52,102–104]. This is primarily due to the influence of the LPBF process where thin features parallel to the build direction have an oversizing propensity dependent on the laser beam size [101,105,106]. Although this effect can be magnified because of the uneven surface at the sub-micron level, this is often advantageous from a tissue engineering perspective.

3.2. Numerical analysis

3.2.1. Model accuracy

The stress-strain curve informed by experimental tests on 3 a.m. samples are shown in Fig. 8a. The curves can be seen to be consistent for

Table 3

CoCrMo bulk material properties informing the numerical model based on experimental tests on fully dense tensile coupons fabricated under identical process parameters to that of the scaffolds.

Material property	Value
Young's modulus (E)	194.23 GPa
Yield strength (σ_y)	975.6 MPa
Poisson's ratio (ν)	0.29
Density (ρ_B)	8300 kg/m^3

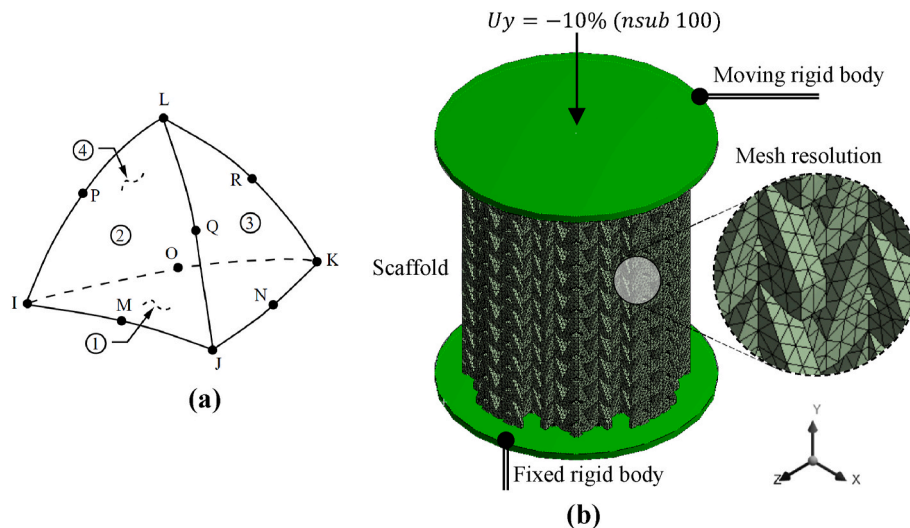


Fig. 4. Numerical simulation illustrating (a) the implementation of a ten-node higher order element type and (b) the application of global loading conditions to determine mechanical performance.

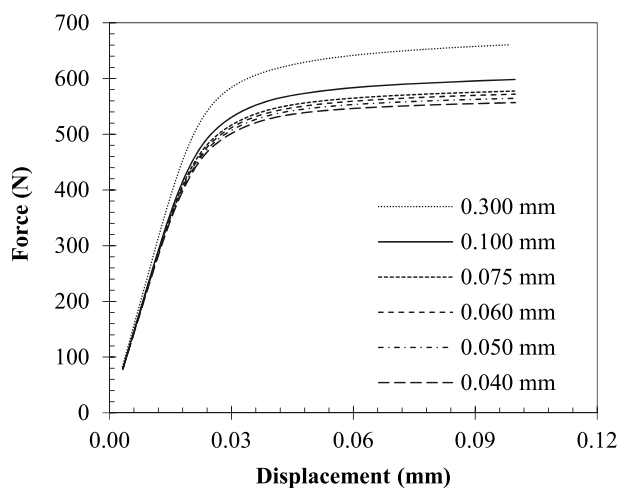


Fig. 5. Influence of mesh size on the force-displacement response.



Fig. 6. Mechanical test setup showing the meta-biomaterial scaffold subject to compressive loading.

the three samples closely following each other signifying a high repeatability for the test data. The accuracy of finite element models is evaluated by comparing their performance up to the yield point (highlighted in green) with equivalent physical test data (EXP), as shown in Fig. 8b. This study focuses on three specific parameters: the elastic modulus (E), the yield strength (σ_y), and the Poisson's ratio (ν), all of which remain unaffected by the post-yield behaviour (highlighted in red). To assess the model's ability to predict these parameters, a mesh convergence analysis was conducted, as shown in Fig. 5. The results indicate a good fit, with differences between the FEA and EXP predicted parameters limited to 2.30–3.84% as listed in Table 5.

Overall, the numerical model closely mirror the elastic behaviour and yield point of the scaffolds. Table 5 compares the numerical and physical test data, namely E , σ_y and $-\nu$ of the meta-biomaterial. The performances show a similar trend between the two methods with the highest difference of 3.84% for σ_y , followed by 2.51% for $-\nu$ and 2.3% for E . Poisson's ratio remained negative signifying auxetic performance for both numerical and physical test cases. Comparing $\sigma - \epsilon$ performances (Fig. 8b) indicates that the numerical model predicts the key mechanical performance parameter at an accuracy of 96.16%.

Although small, the differences observed between the finite element and physical test are due to dimensional deviation observed in the printed sample as informed by the SEM data shown in Fig. 7b. The observations are consistent with literature [22,107–111] confirming a slight shift in dimensions of thin features as a result of the additive manufacturing process. Although these changes are insignificant in thick components, they become prominent in thin-walled structures below 300 μm . The rough surface finish, a distinctive characteristic of Laser powder bed fusion (LPBF) technology [112–114], also has an increasing influence on the mechanical behaviour as the beam thickness reaches sub-micron levels. The comparison of test data revealed reasonable agreement between the finite element model and experimental results, informing its suitability for further analysis.

3.2.2. Stress distribution within the scaffolds

When considering porous materials, the cell structure has a significant impact on the stress distribution. The concentration of stress, which plays a vital role in determining their mechanical behaviour and failure, relies on geometry rather than relative density. Consequently, understanding stress distribution is critical to developing effective design principles. Some architectures are more susceptible to stress concentration, thus contributing to a premature onset of plasticity failure, as per earlier studies [115–119]. However, the link between this

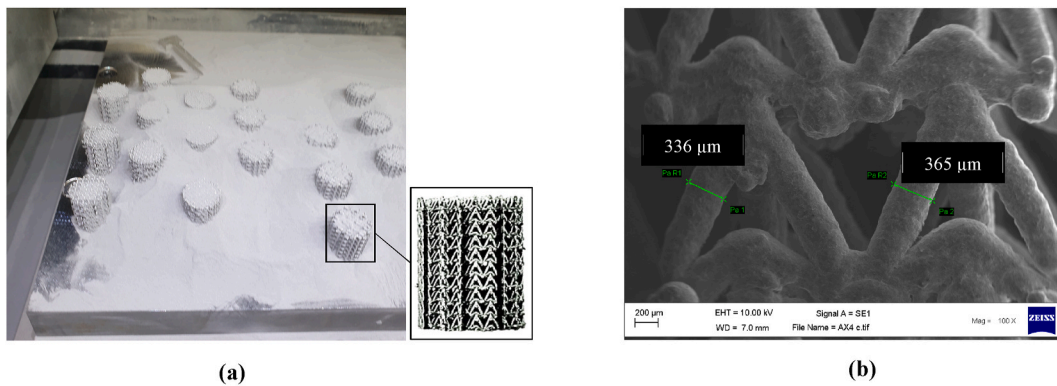


Fig. 7. LPBF CoCrMo meta-biomaterial scaffold showing (a) prototypes on the base plate with geometry highlighted and (b) SEM micrograph of the scaffold showing thickness variation.

Table 4

Difference in porosity observed between the additively manufactured and ideal CAD design of the scaffolds.

Properties	Meta-biomaterial scaffold		
	Ideal	SLM	% Difference
Porosity (%)	86.74	81.98	5.64

phenomenon and auxetic structures, especially in the field of biomedical scaffolds, remains uncertain. In addition, given that scaffolds commonly necessitate a high degree of porosity (>60%), the identification of stress raisers becomes a critical factor in their assessment.

Dissimilar to physical testing, the numerical model generates a copious quantity of information that can be subjected to further analysis provided it is duly validated. As shown in Fig. 9, the stress distribution within the meta-biomaterial scaffold is highlighted, identifying areas of stress concentration. Previous research we conducted [56] has established that the σ_{max} of scaffolds varies significantly based on the unit cell geometry. In this case, the meta-biomaterial displays stress concentration at the joints, with stress distribution appearing relatively uniform throughout the scaffold volume.

3.3. Surrogate model and its accuracy

Response surfaces linking variables t_s and θ_s to the desired responses (v, φ, σ_y and E) are created using surrogate modelling methodology. Before performing parametric analysis, variance analysis is carried out to ensure the accuracy of the models. Using the surrogate modelling methodology, response surfaces that link the variables t_s and θ_s to the responses of interest (v, φ, σ_y and E) are generated. In order to verify the precision of the models, an analysis of variance (ANOVA) [120–122] is carried out prior to their implementation in parametric analysis. The surrogate models are subsequently put to use in ascertaining the correlation between variables and the consequential attributes of the meta-biomaterial. The training matrix used to inform the surrogate model is as shown in Table 6.

Variants of design fulfilling all factorial combinations determined by

Table 5

Difference between the numerical and physical test data.

Properties	FEA	EXP	% Difference
E (GPa)	1.30	1.27	2.30
σ_y (MPa)	50	52	3.84
ν	-0.164	-0.160	2.51

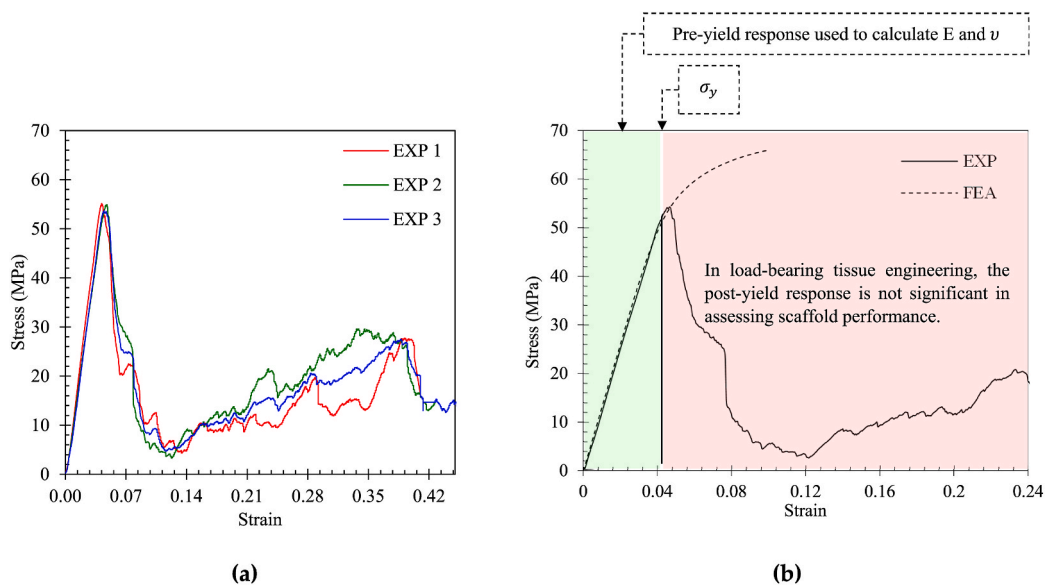


Fig. 8. Stress-strain data for the meta-biomaterial scaffold showing (a) response from physical tests carried out on three samples and (b) comparison between finite element and physical test data.

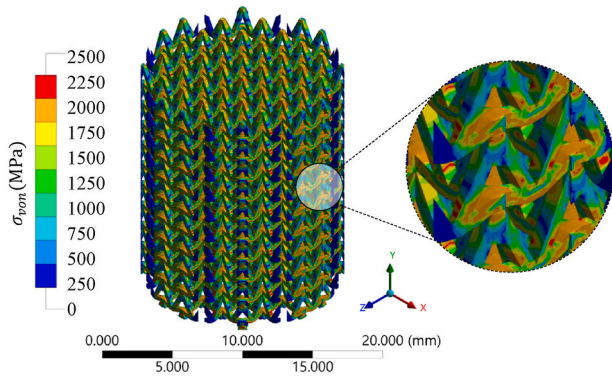


Fig. 9. Numerically informed stress distribution in the auxetic scaffold under axial compression.

Table 6

The geometric variables and responses of interest to train the meta-biomaterial surrogate model.

Factor 1	Factor 2	Response 1	Response 2	Response 3	Response 4
t_s (mm)	θ_s (Deg.)	ν	φ (%)	σ_y (MPa)	E (GPa)
0.39	24	-0.08	80.08	47	10.45
0.43	20	-0.05	77.44	52	14.50
0.47	16	-0.02	75.17	63	18.47
0.43	20	-0.05	77.44	52	14.50
0.43	20	-0.05	77.44	52	14.50
0.43	20	-0.05	77.44	52	14.50
0.43	25	-0.06	77.03	54	14.24
0.43	15	-0.04	78.29	50	13.89
0.39	16	-0.05	81.13	46	10.07
0.47	24	-0.03	73.99	64	18.69
0.43	20	-0.05	77.44	52	14.50
0.48	20	-0.02	73.63	64	20.60
0.38	20	-0.07	81.38	41	09.46

the sampling points are produced. Numerical analysis and modelling of each design sample result in responses as presented in Table 6. This process is crucial as it enables exploration of a broad range of variables and the relationships between them, which can significantly impact scaffold properties. This information can enhance scaffold design and facilitate accurate prediction of its mechanical properties. Moreover, it can also reduce the number of experiments required to achieve the desired results, making the process more cost-effective and efficient.

Upon calculation of the best-fit indicators for the results, it was determined that linear models, as expressed in Eqs. (6)–(8), characterises the porosity, yield strength, and elastic modulus of the meta-biomaterial scaffold. However, it was observed that the parameter ν exhibited a quadratic trend, indicating the presence of interaction effects among the design parameters. This finding is detailed in Eq. (9).

$$\varphi = 115.35 - 81.35t_s - 0.14\theta_s \quad (6)$$

$$\sigma_y = -53.55 + 235.21t_s + 0.27\theta_s \quad (7)$$

$$E = -35.53 + 114.53t_s + 0.04\theta_s \quad (8)$$

$$\nu = 0.59 - 2.42t_s - 0.02\theta_s + 0.04t_s\theta_s + 2.50t_s^2 + 5e^{-5}\theta_s^2 \quad (9)$$

A compendium of the quality metrics utilised to characterise the RS model is furnished in Table 7. It is noteworthy that each of the four models evinces statistically significant outcomes, as is substantiated by their high F-values and correspondingly low p-values, where values below 0.0001 are deemed significant in the realm of surrogate modelling. Moreover, the models exhibit minimal noise, as indicated by the presence of more than four adequate precision ratios, which is a desirable characteristic according to previous studies [79,123–126].

Table 7

ANOVA of the surrogate model that characterises the performance of the meta-biomaterial scaffold.

Model	F-value	p-value	Statistical measurements			
			R ²	Adj-R ²	Pre-R ²	Adeq-precision
φ	1267.76	<0.0001	0.9961	0.9953	0.9920	103.2622
E	613.45	<0.0001	0.9919	0.9903	0.9822	72.873
ν	124.28	<0.0001	0.9889	0.9809	0.9208	37.6713
σ_y	110.16	<0.0001	0.9566	0.9479	0.9130	30.6959

Additionally, all of the models show high R² (>0.9) values, indicating excellent agreement between the anticipated and adjusted R². These findings collectively suggest that all four models are accurate and can be used for further parametric analysis.

Subsequent to ANOVA, scrutiny was directed towards the correlation between the predictions of the FE and surrogate models, as depicted in Fig. 10. Notably, the surrogate model predictions (diagonal dotted line) were observed to be in close proximity to the numerical results for all responses (φ , E , ν and σ_y). The small residuals further confirm the high accuracy of the surrogate model. Thus, the surrogate models are well-suited for predicting the properties and parametric interactions of the meta-biomaterial auxetic scaffold.

The surrogate model presented in this study offers a promising approach for designing stiffness-matched meta-biomaterials with near-zero auxeticity. However, its direct application to non-zero auxetic architectures may require further exploration and adaptation. When stiffness matching is necessary but non-zero auxeticity is desired, the design parameters and optimisation criteria of the surrogate model would need to be adjusted accordingly. The existing model is specifically tailored for achieving near-zero auxeticity, which means it may not directly capture the complexities and requirements of non-zero auxetic structures. To extend the surrogate model to non-zero auxetic architectures, researchers would need to modify the design parameters, such as the geometrical configurations, material composition, or internal lattice structures, to accommodate the desired auxetic behaviour while still maintaining stiffness matching capabilities. This may involve incorporating additional variables or constraints into the optimisation process to achieve the desired balance between auxeticity and stiffness matching. While the surrogate model presented in the study offers a valuable starting point, developing a surrogate model specifically tailored for non-zero auxetic architectures would require dedicated research and experimentation. This could involve iterative refinement and validation through experimental testing, computational simulations, and statistical analyses following the methodology presented in this study.

3.4. Parametric influence on meta-biomaterial characteristics

3.4.1. Porosity

When it comes to the porosity of the meta-biomaterial scaffold being analysed, the strut thickness can be seen to have the highest influence (Fig. 11a). Although not as significant as the auxeticity, it can also be seen to influence the porosity linearly from Fig. 11b. The reduction in strut thickness leads to a linear increase in porosity, as depicted in Fig. 11a. Similarly, a comparable pattern was observed for θ_s , but with a considerably lower linear slope.

The interaction effects of the design parameters were subjected to analysis, and as portrayed in Fig. 11c, the least porosity value of 73.63% was noted at the highest values of t_s and θ_s . Furthermore, the trend for the interaction effect persisted at the highest porosity of 81.38%, where the lowest values of t_s and θ_s were used. Consequently, reducing the thickness decreases the relative density of the meta-biomaterial scaffold, resulting in a higher porosity. On the other hand, decreasing θ_s reduces the strut length, leading to an increased relative density, which impacts porosity at a lower rate than t_s . Moreover, an interdependence between

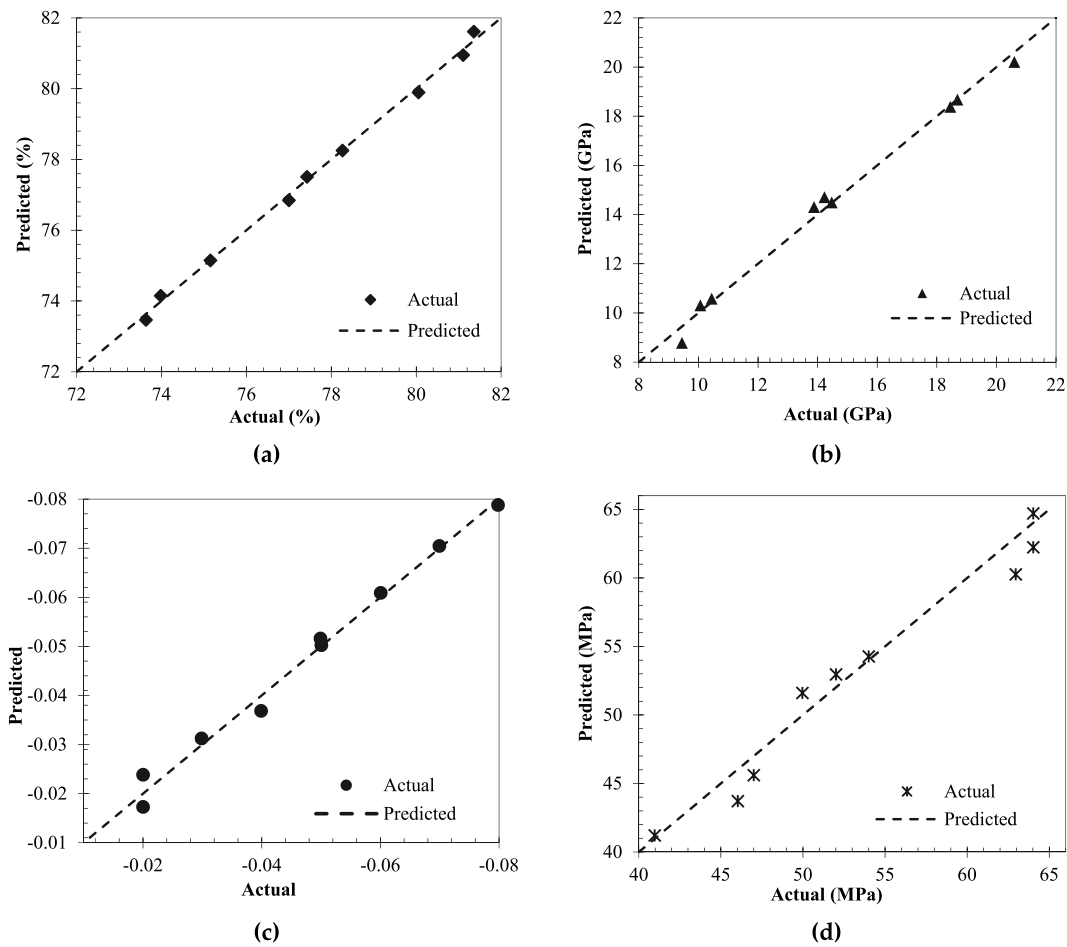


Fig. 10. Show the accuracy of the surrogate and FE results of the meta-biomaterial for (a) Porosity, (b) elastic modulus, (c) Poisson's ratio and (d) Yield strength.

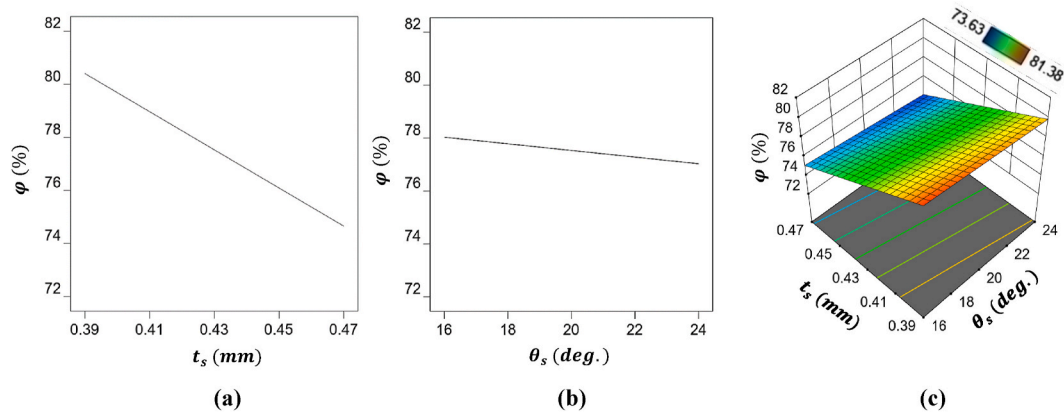


Fig. 11. Showing how geometric factors affect the meta-biomaterial characteristics revealing (a) the effect of strut width on porosity, (b) the impact of strut inclination on porosity, and (c) the correlation between width and inclination.

t_s and θ_s on porosity is also visible in Fig. 11c. As a result, varying t_s can significantly alter the porosity of the meta-biomaterial. Overall, the primary factor influencing porosity is t_s , as seen in the first-order effects. Therefore, reducing t_s will result in higher porosity than reducing equal measures of θ_s .

3.4.2. Stiffness

The stiffness of the meta-biomaterial scaffold primarily depends on t_s (Fig. 12a), with the highest and lowest values of E (20.6 GPa and 9.46 GPa, respectively) corresponding to the highest and lowest t_s ,

respectively. On the other hand, the effect of θ_s on the elastic modulus is insignificant, as shown by a nearly straight line across all tested angles in Fig. 12b. As a result, t_s is the most critical factor in determining the elastic modulus of the scaffold investigated in the meta-biomaterial architecture. This correlation is not unexpected, as the thickness was discovered to have a significant impact on the structure's relative density. Furthermore, Fig. 12c demonstrates that the interrelationship between the design parameters and E is minimal and has no impact on the performance pattern, resulting in a consistent performance slope regardless of θ_s variations. As a result, increasing t_s is the only method

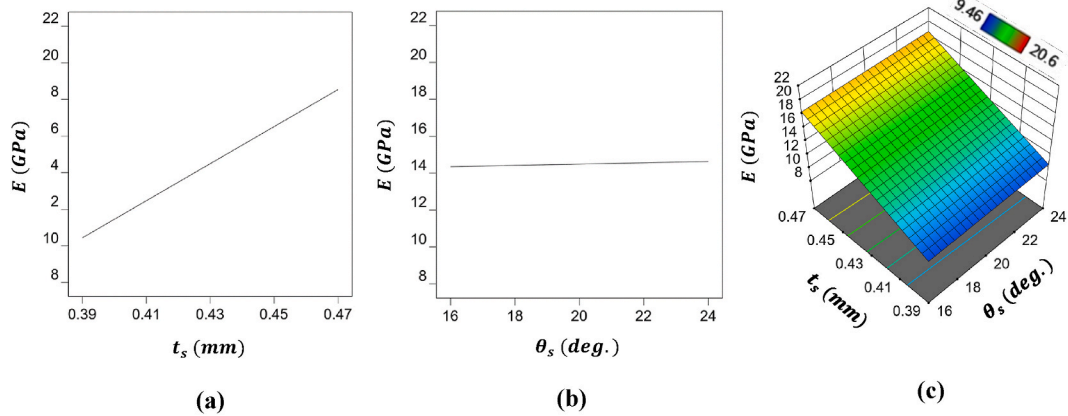


Fig. 12. Showing how geometric factors affect the meta-biomaterial characteristics revealing (a) the effect of strut width on elastic modulus, (b) the impact of strut inclination on elastic modulus, and (c) the correlation between width and inclination.

for increasing the elastic modulus of the meta-biomaterial architecture. This observation is consistent with porous materials, where the stiffness is primarily related to the amount of material retained [70,127,128]. Therefore, for the meta-biomaterial scaffold under consideration, increasing the thickness will increase the relative density, ultimately resulting in a stiffer architecture and higher elastic modulus.

3.4.3. Poisson's ratio

The results presented in Fig. 13 indicate that both t_s and θ_s have a significant impact on the $-\nu$. In Fig. 13a, a quadratic relationship can be observed, with the absolute value of $-\nu$ increasing as thickness increases. This is due to the porosity allowing space for the double-arrowhead cellular layers to contract, which significantly influences lateral shrinkage. As thickness increases, the relative density decreases, leading to a higher stiffness and reduced elastic deformation. Consequently, lateral shrinkage is reduced, increasing the absolute value of $-\nu$. As shown in Fig. 13b, both design parameters significantly affect the value of $-\nu$.

An increase in strut angle leads to more load being transferred to the lateral connections, resulting in increased lateral strain and, therefore, increased $-\nu$. Additionally, reducing θ_s below a specific threshold causes a transition from negative to positive Poisson's ratio. The findings in Fig. 13c demonstrate that decreasing t_s and increasing θ_s lead to a rise in $-\nu$, with the highest value achieved at the highest angle and lowest thickness. Furthermore, t_s has a greater impact on $-\nu$ than θ_s . Finally, the interaction effect of t_s and θ_s has the least significant effect. Based on

these results, it can be concluded that the first-order effect of t_s is the most influential factor in altering the $-\nu$ of the meta-biomaterial, followed by θ_s and, finally, the interaction effect of t_s and θ_s .

3.4.4. Yield strength

Fig. 14a demonstrates that the thickness of the strut has a dominant influence on the scaffold's strength. The relationship between strength and strut thickness is linear. Fig. 14b illustrates that an increase in θ_s results in a proportional increase in strength. However, the rate of increase for θ_s is notably lower than that of t_s . Fig. 14c presents the interdependence of both θ_s and t_s on the meta-biomaterial strength. Although both θ_s and t_s are sensitive to strength, the increase is mainly offered by t_s , which exhibits a linear pattern with a minor contribution from θ_s . Nevertheless, the interaction effects indicate that the maximum strength occurs when both t_s and θ_s are at their highest values. Consequently, t_s has the most significant impact on strength, followed by θ_s in the order of $t_s > \theta_s$.

3.5. Stiffness matched meta-biomaterial

The problem description for stiffness matching the meta-biomaterial scaffold with that of a host bone is created by conceiving an objective function. To achieve the objective function, the design variables must be modified while adhering to their boundaries. The identification of optimal design parameters for targeted performance requires defining a suitable problem description. In this scenario, the ideal meta-

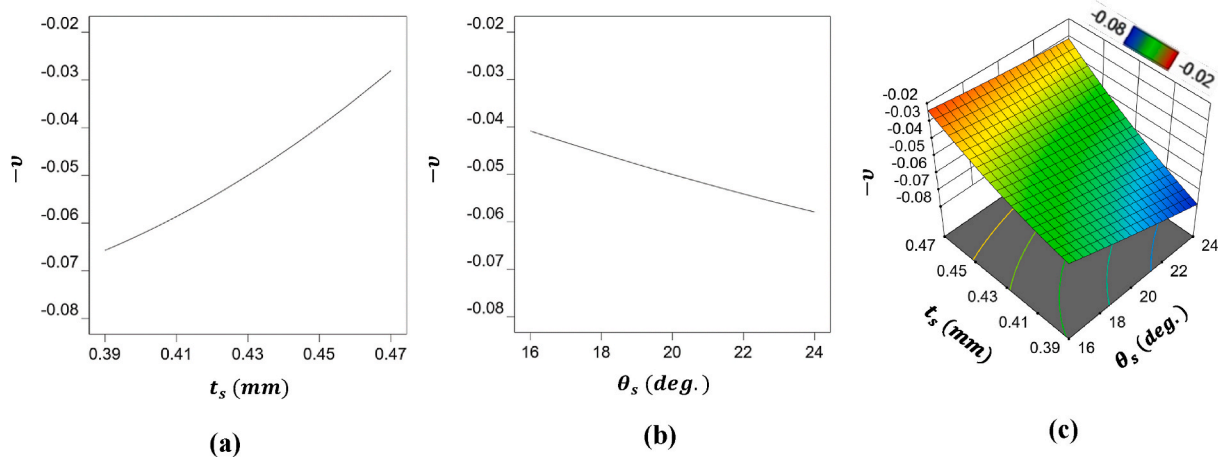


Fig. 13. Showing how geometric factors affect the meta-biomaterial characteristics revealing (a) the effect of strut width on Poisson's ratio, (b) the impact of strut inclination on Poisson's ratio, and (c) the correlation between width and inclination.

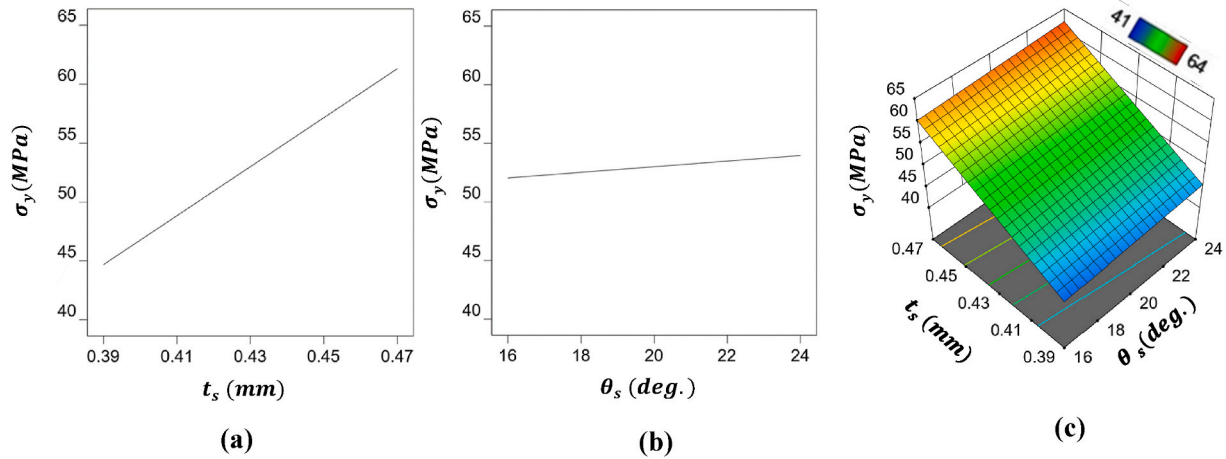


Fig. 14. Showing how geometric factors affect the meta-biomaterial characteristics revealing (a) the effect of strut width on strength, (b) the impact of strut inclination on strength, and (c) the correlation between width and inclination.

biomaterial scaffold should satisfy various criteria. Firstly, it must possess a $-v$ close to zero and stiffness of 18 GPa. The stiffness value is chosen to match with that of an adult cortical bone, thereby preventing stress shielding and maladapted stress concentration [56]. Additionally, it is crucial to maximise the yield strength while maintaining high porosity to provide optimal compressive strength and support bone reintegration. In this regard, the multi-objective criteria for the stiffness matched near zero $-v$ meta-biomaterial scaffold considering all the relevant parameters can be conceived as shown in Eq. (10):

$$\begin{cases}
 \text{Maximise } \sigma_y = f_1(\theta_s, t_s) \\
 \text{Maximise } \varphi = f_2(\theta_s, t_s) \\
 \text{Maximise } -v = f_3(\theta_s, t_s) \\
 \text{s.t. } E = 18 \text{ GPa} \\
 \text{s.t. } 15.0 \leq \theta_s \leq 25.0 \\
 \text{s.t. } 0.38 \leq t_s \leq 0.48
 \end{cases} \quad (10)$$

To transform the optimisation solution into a desirability function that outlines the acceptable response ranges for each response d_i , a desirability criterion $D(X)$ is used, as illustrated in Eq. (11):

$$D = (d_1 \cdot d_2 \cdot \dots \cdot d_n)^{\frac{1}{n}} = \left(\prod_{i=1}^n d_i \right)^{\frac{1}{n}} \quad (11)$$

where, n is the number of responses. To ensure simultaneous optimisation, each response was assigned a low and high value, as specified in Eq. (11), and solved using the desirability approach. The optimisation output is visualized in Fig. 15, which depicts the desirability objective as a function of the meta-biomaterial's strut angle and thickness. The highest achievable desirability of 0.94 was attained at a strut angle and thickness as listed in Table 8. This result provides valuable insights into the optimal design parameters for the meta-biomaterial, enabling the development of more efficient and effective biomaterials for various biomedical applications.

In Fig. 15, the highest desirability score of 0.94 is observed at the highest values of thickness and angle. Based on this information, a meta-biomaterial scaffold design meeting the topmost desirability criterion was generated and characterised numerically, as shown in Fig. 16 and Table 8. The von-Mises stress contour depicted in Fig. 16 indicates a robust scaffold, while the optimal features listed in Table 9. Upon evaluation, the surrogate model underestimated $-v$ and φ by 2.7% and 0.39%, respectively, while overestimating E and σ_y by 4.39% and 2.27%, respectively. These results demonstrate that the optimal design provides

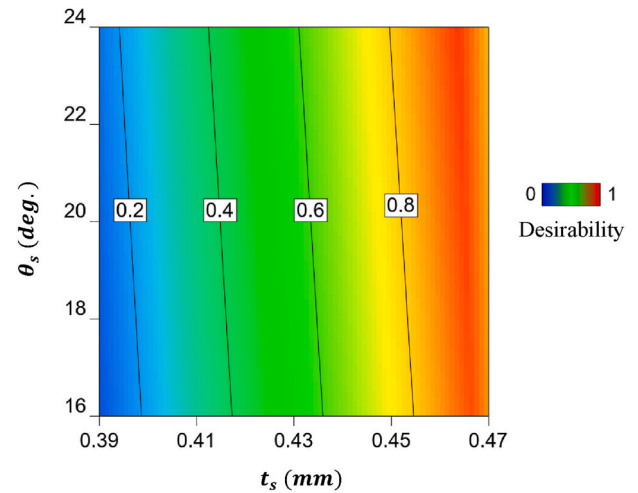


Fig. 15. The desirability of the optimum solution delivering stiffness matching and near zero Poisson's ratio against design variables for the meta-biomaterial scaffold.

Table 8

Predicted optimal solution for the meta-biomaterial meeting all the desirability criteria including stiffness matching and near zero Poisson's ratio.

Number	t_s (mm)	θ_s (Deg.)	Desirability
1	0.459	23.53	0.94

a scaffold that offer near-zero auxetic performance (≤ 0.037), and stiffness-matching.

While previous literature [4,129] has explored meta-biomaterials with negative and positive Poisson's ratios within a similar porosity range of $75 \pm 1\%$, this study presents the first investigation into a CoCrMo meta-biomaterial with a near-zero Poisson's ratio. The performance comparison, as shown in Fig. 17, demonstrates that the surrogate model developed in this research can generate meta-biomaterial architectures that exhibit significantly enhanced performance. Specifically, the surrogate model yields architectures that outperform other comparable CoCrMo architectures by a minimum of nine times in terms of elastic modulus (Fig. 17a). Similarly, when examining yield strength (Fig. 17b), this study surpasses the performance of Ghani et al. [129] by approximately 34%. These findings highlight the capability of the surrogate model to conceive meta-biomaterials with superior mechanical

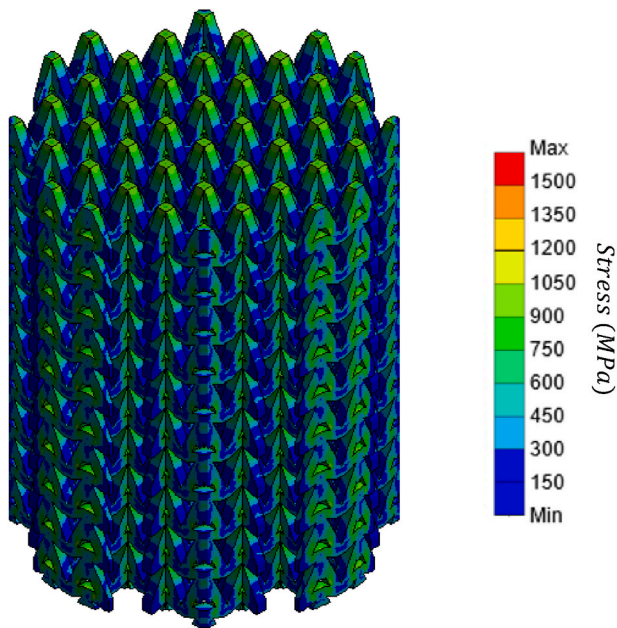


Fig. 16. Stress distribution of the stiffness matched meta-biomaterial satisfying the desirability criterion.

Table 9

Comparison of predicted and numerically analysed performance of the stiffness-matched optimum meta-biomaterial showing Poisson's ratio, porosity, elastic modulus E (GPa) and Yield strength σ_y (MPa).

Item	ν	φ	E	σ_y
Predicted	-0.036	74.63	18	60.88
FEM	-0.037	74.93	17.21	59.5
% Difference	2.7	0.39	4.39	2.27

properties, positioning it as a promising approach for future investigations.

The outcomes of this inquiry affirm the precision of the surrogate model in evaluating the mechanical behaviour of the double-arrowhead meta-biomaterial, with a success rate of 95.6%. The response surface modelling technique has enormous potential for developing auxetic bone scaffolds with specific functionalities. The findings provide valuable insights for researchers and engineers to develop and manufacture biomaterials with targeted mechanical properties and behaviours, ultimately leading to the creation of more efficient biomaterials for diverse biomedical applications and improving patient health.

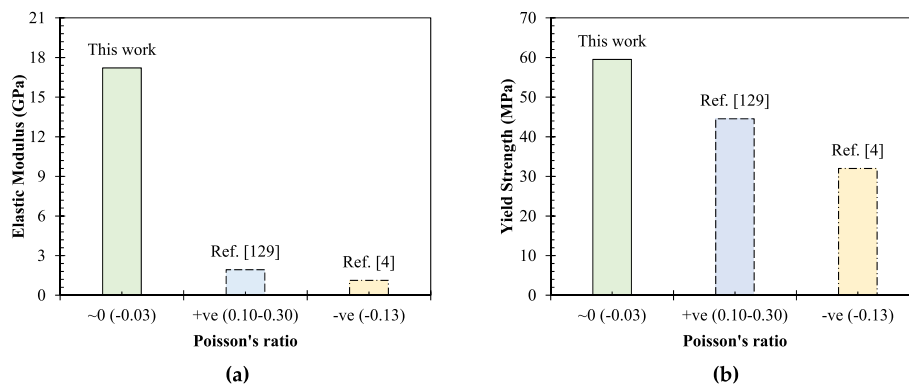


Fig. 17. Performance of near zero (~ 0) CoCrMo meta-biomaterials featuring comparable porosity ($75 \pm 1\%$) showing (a) comparison of elastic modulus and (b) yield strength with other attempts from literature [4,129] featuring negative (-ve) and positive (+ve) Poisson's ratios.

3.6. Prospects and potential for future work

AM of customised stiffness-matched meta-biomaterials opens up several avenues for future research and holds prospects in the field of bone tissue engineering and biomedical devices. The surrogate model developed in this study serves as a valuable tool for generating personalised scenarios for the production of bone scaffolds. By refining and expanding the surrogate model, incorporating additional design parameters, and optimising the meta-biomaterial architecture for specific tissue repair applications, researchers can further enhance the performance and functionality of these scaffolds. Whilst the current study utilised CoCrMo alloy, other materials such as titanium alloys or biodegradable polymers can be explored, either individually or in combination, for multi-material printing. Incorporating multiple materials with tailored properties can further enhance the functionality and performance of the meta-biomaterial scaffolds. Understanding the effect of material composition on mechanical behaviour, degradation kinetics, and biological response will provide valuable insights for future designs. Advancements in printing techniques and post-processing methods are also worth exploring. Although the current focus was on L-PBF, other advanced 3D printing techniques can be investigated to fabricate meta-biomaterial scaffolds with improved resolution and control over the internal architecture. Post-processing techniques such as surface modification, coating deposition, or functionalisation can also be explored to enhance the bioactivity, antibacterial properties, or drug delivery capabilities of the meta-biomaterial scaffolds.

To bring the research closer to clinical applications, future work should focus on clinical translation and customisation. This involves translating the optimised meta-biomaterial designs into scalable manufacturing processes, ensuring regulatory compliance, and conducting preclinical and clinical studies to validate their efficacy and safety in human patients. Developing efficient and cost-effective manufacturing workflows, including patient-specific design and fabrication, will be crucial in realising the full potential of this technology. There is also potential for the concept of stiffness-matching to be extended beyond load-bearing tissue repair. Researchers can explore the potential of these meta-biomaterials in cartilage regeneration, ligament and tendon repair, and even organ engineering. By expanding the application scope, this technology has the potential to revolutionise tissue engineering, enabling highly tailored and effective treatments across various fields. Overall, the potential for future work and prospects in this area are extensive, ranging from optimising design and assessing biocompatibility to exploring new materials and printing techniques. With continued research and development, this technology has the potential to transform load-bearing tissue reconstruction and contribute to the advancement of tissue engineering as a whole.

3.7. Challenges for commercial use

For meta-biomaterials to be commonplace in tissue reconstruction, multiple limitations require addressing. When it comes to additive manufacturing, structural integrity at the sub-micron scales suitable for the fabrication of meta-biomaterials remains a primary limitation. Furthermore, improvements in reducing contamination during fabrication and post-processing are also necessary. While the latest L-PBF technique meets the basic requirements for the fabrication of meta-biomaterials, there is still a need for achieving smaller dimensions, improved dimensional accuracy, and consistent mechanical properties to streamline the integration of AM meta-biomaterials into a clinical setting. In addition to manufacturing, there are also design-related challenges: For instance, the limited literature on meta-biomaterials means that it is not often clear what exact geometries would give rise to the most desired properties for a given scenario. Given that stiffness matching between the meta-biomaterial and the host tissue is one of the primary considerations for bone scaffolds, there is a need for computational models that offer the relationship between geometrical designs and the resulting properties of meta-biomaterials. The growth of literature addressing these key limitations are critical in taking meta-biomaterial research into clinical practice.

4. Conclusion

In this investigation, the utilization of laser powder bed fusion is disclosed for the purpose of producing CoCrMo meta-biomaterials offering near-zero negative Poisson's ratio ($-v$) and precise stiffness (E) matching. A surrogate framework for auxetic meta-biomaterial that can anticipate the trend in $-v$, porosity (φ), strength (σ_y), and elastic modulus (E) under the influence of design variables such as strut thickness (t_s) and auxetic angle (θ_s). This technique allows for the fabrication of meta-biomaterials possessing tailored properties that are well-suited for load-bearing tissue engineering purposes. The meta-biomaterial architecture produced in this research provides $-v$, φ , σ_y and E ranging from -0.02 to -0.08 , 73.63–81.38%, 41–64 MPa, and 9.46–20.6 GPa, respectively. The most favorable meta-biomaterial solution displays a nearly zero $-v$ of 0.037 and a targeted E of 17.21 GPa, while also demonstrating σ_y and φ of 59.5 MPa and 74.93%, respectively. The parametric analysis discovered a linear correlation between φ and E , with t_s exerting a more significant influence than θ_s . All parametric combinations exhibited auxetic performance concerning $-v$, displaying a quadratic connection to design variables. However, the σ_y , φ , and E showed a linear relationship with the design variables. In terms of the influence of design parameters, the order of impact reveals that the meta-biomaterial properties are predominantly affected by the first-order effects of t_s and θ_s , specifically $t_s > \theta_s$, with their interdependence ($t_s\theta_s$) only being significant for $-v$. The findings of this study indicate that it is indeed possible to develop CoCrMo auxetic bone scaffolds that possess targeted stiffness characteristics and an almost zero Poisson's ratio. The surrogate model developed through this research can be utilised to facilitate the design and fabrication of such scaffolds with a high degree of accuracy and efficiency. This promising development holds great potential for the advancement of biomaterials and tissue engineering. By creating scaffolds with customised mechanical properties, researchers and clinicians can develop more effective treatments for a range of conditions and injuries. This, in turn, may lead to better clinical outcomes and improved quality of life for patients in need.

CRedit authorship contribution statement

Chameekara T. Wanniarachchi: Conceptualization, Methodology, Software, Investigation, Validation, Formal analysis, Writing – original draft, Writing – review & editing. **Arun Arjunan:** Conceptualization, Supervision, Methodology, Software, Investigation, Validation, Formal

analysis, Writing – original draft, Writing – review & editing. **Ahmad Baroutaji:** Conceptualization, Methodology, Software, Investigation, Validation, Formal analysis, Writing – original draft, Writing – review & editing. **Manpreet Singh:** Software, Investigation, Validation, Formal analysis.

Declaration of competing interest

The authors declare that they have no known competing financial interests or personal relationships that could have appeared to influence the work reported in this paper.

Data availability

Data will be made available on request.

References

- [1] A.A. Zadpoor, Mechanical Performance of Additively Manufactured Meta-Biomaterials, Acta Materialia Inc, 2019, <https://doi.org/10.1016/j.actbio.2018.12.038>.
- [2] M. Szymoniuk, M. Mazurek, A. Dryla, P. Kamieniak, M. Tilton, E. Jacobs, R. Overdorff, M. Astudillo Potes, L. Lu, G. Manogharan, S. Vyavahare, V. V. Mahesh, V.V. Mahesh, D. Harursampath, Biomechanical behavior of PMMA 3D printed biomimetic scaffolds: effects of physiologically relevant environment, Exp. Neurol. 138 (2023), 114366, <https://doi.org/10.1016/j.compstruct.2022.116491>.
- [3] M. Szymoniuk, M. Mazurek, A. Dryla, P. Kamieniak, The application of 3D-bio-printed scaffolds for neuronal regeneration after traumatic spinal cord injury – a systematic review of preclinical in vivo studies, Exp. Neurol. 363 (2023), 114366, <https://doi.org/10.1016/j.expneurol.2023.114366>.
- [4] C.T. Wanniarachchi, A. Arjunan, A. Baroutaji, M. Singh, Mechanical performance of additively manufactured cobalt-chromium-molybdenum auxetic meta-biomaterial bone scaffolds, J. Mech. Behav. Biomed. Mater. 134 (2022), 105409, <https://doi.org/10.1016/j.jmbbm.2022.105409>.
- [5] Z. Jia, X. Xu, D. Zhu, Y. Zheng, Design, printing, and engineering of regenerative biomaterials for personalized bone healthcare, Prog. Mater. Sci. 134 (2023), 101072, <https://doi.org/10.1016/j.pmatsci.2023.101072>.
- [6] H. Xiao, X. Chen, X. Liu, G. Wen, Y. Yu, Recent advances in decellularized biomaterials for wound healing, Mater. Today Bio. 19 (2023), 100589, <https://doi.org/10.1016/j.mtbio.2023.100589>.
- [7] G. Flamourakis, I. Spanos, Z. Vangelatos, P. Manganas, L. Papadimitriou, C. Grigoropoulos, A. Ranella, M. Farsari, Laser-made 3D auxetic metamaterial scaffolds for tissue engineering applications, Macromol. Mater. Eng. 305 (2020), 2000238, <https://doi.org/10.1002/mame.202000238>.
- [8] Y. Jin, C. Xie, Q. Gao, X. Zhou, G. Li, J. Du, Y. He, Fabrication of multi-scale and tunable auxetic scaffolds for tissue engineering, Mater. Des. 197 (2021), 109277, <https://doi.org/10.1016/j.matdes.2020.109277>.
- [9] A.A. Zadpoor, Bone tissue regeneration: the role of scaffold geometry, Biomater. Sci. 3 (2015) 231–245, <https://doi.org/10.1039/C4BM00291A>.
- [10] E.A. Casanova, A. Rodriguez-Palomo, L. Stähli, K. Arnke, O. Gröniger, M. Generali, Y. Neldner, S. Tiziani, A.P. Dominguez, M. Guizar-Sicairos, Z. Gao, C. Appel, L.C. Nielsen, M. Georgiadis, F.E. Weber, W. Stark, H.-C. Pape, P. Cinelli, M. Liebi, SAXS imaging reveals optimized osseointegration properties of bioengineered oriented 3D-PLGA/aCaP scaffolds in a critical size bone defect model, Biomaterials 294 (2023), 121989, <https://doi.org/10.1016/j.biomaterials.2022.121989>.
- [11] E.E. Huang, N. Zhang, E.A. Ganio, H. Shen, X. Li, M. Ueno, T. Utsunomiya, M. Maruyama, Q. Gao, N. Su, Z. Yao, F. Yang, B. Gaudillière, S.B. Goodman, Differential dynamics of bone graft transplantation and mesenchymal stem cell therapy during bone defect healing in a murine critical size defect, J. Orthop. Transl. 36 (2022) 64–74, <https://doi.org/10.1016/j.jot.2022.05.010>.
- [12] C. Polley, W. Radlof, F. Hauschulz, C. Benz, M. Sander, H. Seitz, Morphological and mechanical characterisation of three-dimensional gyroid structures fabricated by electron beam melting for the use as a porous biomaterial, J. Mech. Behav. Biomed. Mater. 125 (2022), 104882, <https://doi.org/10.1016/j.jmbbm.2021.104882>.
- [13] A. Bédier, M. Genta, N. Kunz, C. Verheyen, M. Martins, J. Brefre-Guth, T. Braschler, Design of an elastic porous injectable biomaterial for tissue regeneration and volume retention, Acta Biomater. 142 (2022) 73–84, <https://doi.org/10.1016/j.actbio.2022.01.050>.
- [14] L. Zhang, B. Song, L. Yang, Y. Shi, Tailored mechanical response and mass transport characteristic of selective laser melted porous metallic biomaterials for bone scaffolds, Acta Biomater. 112 (2020) 298–315, <https://doi.org/10.1016/j.actbio.2020.05.038>.
- [15] A. Arjunan, A. Baroutaji, J. Robinson, A.S. Praveen, A. Pollard, C. Wang, Future directions and requirements for tissue engineering biomaterials, in: Ref. Modul. Mater. Sci. Mater. Eng., Elsevier, 2021, <https://doi.org/10.1016/B978-0-12-815732-9.00068-1>.

- [16] A.H. Foroughi, M.J. Razavi, Shape optimization of orthopedic porous scaffolds to enhance mechanical performance, *J. Mech. Behav. Biomed. Mater.* 128 (2022), 105098, <https://doi.org/10.1016/j.jmbbm.2022.105098>.
- [17] B.M. Ferguson, A. Entezari, J. Fang, Q. Li, Optimal placement of fixation system for scaffold-based mandibular reconstruction, *J. Mech. Behav. Biomed. Mater.* 126 (2022), 104855, <https://doi.org/10.1016/j.jmbbm.2021.104855>.
- [18] K. Cheikho, C. Laurent, J.F. Ganghoffer, An advanced method to design graded cylindrical scaffolds with versatile effective cross-sectional mechanical properties, *J. Mech. Behav. Biomed. Mater.* 125 (2022), 104887, <https://doi.org/10.1016/j.jmbbm.2021.104887>.
- [19] D. Xia, Y. Qin, H. Guo, P. Wen, H. Lin, M. Voshage, J.H. Schleifenbaum, Y. Cheng, Y. Zheng, Additively manufactured pure zinc porous scaffolds for critical-sized bone defects of rabbit femur, *Bioact. Mater.* 19 (2023) 12–23, <https://doi.org/10.1016/j.bioactmat.2022.03.010>.
- [20] X. Wang, S. Xu, S. Zhou, W. Xu, M. Leary, P. Choong, M. Qian, M. Brandt, Y. Xie, Topological design and additive manufacturing of porous metals for bone scaffolds and orthopaedic implants: a review, *Biomaterials* 83 (2016) 127–141, <https://doi.org/10.1016/j.biomaterials.2016.01.012>.
- [21] D.J. Rosario, G.C. Reilly, E.A. Salah, M. Glover, A.J. Bullock, S. MacNeil, Decellularization and sterilization of porcine urinary bladder matrix for tissue engineering in the lower urinary tract, *Regen. Med.* 3 (2008) 145–156, <https://doi.org/10.2217/17460751.3.2.145>.
- [22] F. Liu, Z. Mao, P. Zhang, D.Z. Zhang, J. Jiang, Z. Ma, Functionally graded porous scaffolds in multiple patterns: new design method, physical and mechanical properties, *Mater. Des.* 160 (2018) 849–860, <https://doi.org/10.1016/j.matdes.2018.09.053>.
- [23] W.S. Tan, A.C. Moore, M.M. Stevens, Minimum design requirements for a poroelastic mimic of articular cartilage, *J. Mech. Behav. Biomed. Mater.* 137 (2023), 105528, <https://doi.org/10.1016/j.jmbbm.2022.105528>.
- [24] A. Rawal, S. Sharma, D. Singh, N.K. Jangir, H. Saraswat, D. Sebök, A. Kukovec, D. Hietel, M. Dauner, L. Onal, Out-of-plane auxetic nonwoven as a designer meta-biomaterial, *J. Mech. Behav. Biomed. Mater.* (2020), 104069, <https://doi.org/10.1016/j.jmbbm.2020.104069>.
- [25] J.J. Warner, A.R. Gillies, H.H. Hwang, H. Zhang, R.L. Lieber, S. Chen, 3D-printed biomaterials with regional auxetic properties, *J. Mech. Behav. Biomed. Mater.* 76 (2017) 145–152, <https://doi.org/10.1016/j.jmbbm.2017.05.016>.
- [26] A.A. Zadpoor, Meta-biomaterials, *Biomater. Sci.* 8 (2020) 18–38, <https://doi.org/10.1039/c9bm01247h>.
- [27] R. Hedayati, M. Sadighi, M. Mohammadi-Aghdam, A.A. Zadpoor, Mechanics of additively manufactured porous biomaterials based on the rhombicuboctahedron unit cell, *J. Mech. Behav. Biomed. Mater.* 53 (2016) 272–294, <https://doi.org/10.1016/j.jmbbm.2015.07.013>.
- [28] B. Florijn, C. Coullais, M. Van Hecke, Programmable mechanical metamaterials, *Phys. Rev. Lett.* 113 (2014), <https://doi.org/10.1103/PhysRevLett.113.175503>.
- [29] J. Christensen, M. Kadic, O. Kraft, M. Wegener, Vibrant times for mechanical metamaterials, *MRS Commun* 5 (2015) 453–462, <https://doi.org/10.1557/mrc.2015.51>.
- [30] Z. Liu, M.A. Meyers, Z. Zhang, R.O. Ritchie, Functional gradients and heterogeneities in biological materials: design principles, functions, and bioinspired applications, *Prog. Mater. Sci.* 88 (2017) 467–498, <https://doi.org/10.1016/j.pmatsci.2017.04.013>.
- [31] S. Babaee, J. Shim, J.C. Weaver, E.R. Chen, N. Patel, K. Bertoldi, 3D soft metamaterials with negative Poisson's ratio, *Adv. Mater.* 25 (2013) 5044–5049, <https://doi.org/10.1002/adma.201301986>.
- [32] N. Ghavidelnia, M. Bodaghi, Reza Hedayati, Femur auxetic meta-implants with tuned micromotion distribution, *Materials* (2021) 1–29.
- [33] A.A. Zadpoor, Current trends in metallic orthopedic biomaterials: from additive manufacturing to bio-functionalization, infection prevention, and beyond, *Int. J. Mol. Sci.* 19 (2018), <https://doi.org/10.3390/ijms19092684>.
- [34] F. Scarpa, Auxetic materials for bioprostheses [In the Spotlight], *IEEE Signal Process. Mag.* 25 (2008) 126–128, <https://doi.org/10.1109/MSP.2008.926663>.
- [35] F.S.L. Bobbert, S. Janbaz, A.A. Zadpoor, Towards deployable meta-implants, *J. Mater. Chem. B* 6 (2018) 3449–3455, <https://doi.org/10.1039/c8tb00576a>.
- [36] M. Shirzad, A. Zolfagharian, M. Bodaghi, S.Y. Nam, Auxetic metamaterials for bone-implanted medical devices: recent advances and new perspectives, *Eur. J. Mech. Solid.* 98 (2023), 104905, <https://doi.org/10.1016/j.euromechsol.2022.104905>.
- [37] Y. Jiang, K. Shi, L. Zhou, M. He, C. Zhu, J. Wang, J. Li, Y. Li, L. Liu, D. Sun, G. Feng, Y. Yi, L. Zhang, 3D-printed auxetic-structured intervertebral disc implant for potential treatment of lumbar herniated disc, *Bioact. Mater.* 20 (2023) 528–538, <https://doi.org/10.1016/j.bioactmat.2022.06.002>.
- [38] M. Balan P, J. Mertens A, M.V.A.R. Bahubalendruni, Auxetic mechanical metamaterials and their futuristic developments: a state-of-art review, *Mater. Today Commun.* 34 (2023), 105285, <https://doi.org/10.1016/j.mtcomm.2022.105285>.
- [39] A.K. Menon, S.J. Kalita, Porous scaffolds using nanocrystalline titania for bone graft applications, in: *Adv. Bioceram. Porous Ceram. II*, John Wiley & Sons, Ltd, 2009, pp. 191–201, <https://doi.org/10.1002/9780470584354.ch18>.
- [40] A.-M. Yousefi, M.E. Hoque, R.G.S. V Prasad, N. Uth, Current strategies in multiphasic scaffold design for osteochondral tissue engineering: a review, *J. Biomed. Mater. Res., Part A* 103 (2015) 2460–2481, <https://doi.org/10.1002/jbm.a.35356>.
- [41] Y. Chen, M.-H. Fu, Mechanical properties of a novel zero Poisson's ratio honeycomb, *Adv. Eng. Mater.* 20 (2018), 1700452, <https://doi.org/10.1002/adem.201700452>.
- [42] P. Soman, D.Y. Fozdar, J.W. Lee, A. Phadke, S. Varghese, S. Chen, A three-dimensional polymer scaffolding material exhibiting a zero Poisson's ratio, *Soft Matter* 8 (2012) 4946–4951, <https://doi.org/10.1039/c2sm07354d>.
- [43] H.M.A. Kolken, S. Janbaz, S.M.A. Leeftang, K. Lietaert, H.H. Weinsan, A. A. Zadpoor, Rationally designed meta-implants: a combination of auxetic and conventional meta-biomaterials, *Mater. Horiz.* 5 (2018) 28–35, <https://doi.org/10.1039/C7MH00699C>.
- [44] X. Niu, N. Li, Z. Du, X. Li, Integrated gradient tissue-engineered osteochondral scaffolds: challenges, current efforts and future perspectives, *Bioact. Mater.* 20 (2023) 574–597, <https://doi.org/10.1016/j.bioactmat.2022.06.011>.
- [45] B.C. Palivela, S.D. Bandari, R.S. Mamilla, Extrusion-based 3D printing of bioactive glass scaffolds—process parameters and mechanical properties: a review, *Bioprinting* 27 (2022), e00219, <https://doi.org/10.1016/j.bprint.2022.e00219>.
- [46] W. Bian, D. Li, Q. Lian, X. Li, W. Zhang, K. Wang, Z. Jin, Fabrication of a bio-inspired beta-Tricalcium phosphate/collagen scaffold based on ceramic stereolithography and gel casting for osteochondral tissue engineering, *Rapid Prototyp. J.* 18 (2012) 68–80, <https://doi.org/10.1108/13552541211193511>.
- [47] M. Tarik Ararat, I. Gibson, X. Li, State of the art and future direction of additive manufactured scaffolds-based bone tissue engineering, *Rapid Prototyp. J.* 20 (2014) 13–26, <https://doi.org/10.1108/RPJ-03-2012-0023>.
- [48] F. Sun, T. Wang, Y. Yang, Hydroxyapatite composite scaffold for bone regeneration via rapid prototyping technique: a review, *Rapid Prototyp. J.* 28 (2022) 585–605, <https://doi.org/10.1108/RPJ-09-2020-0224>.
- [49] J. Wieding, A. Wolf, R. Bader, Numerical optimization of open-porous bone scaffold structures to match the elastic properties of human cortical bone, *J. Mech. Behav. Biomed. Mater.* 37 (2014) 56–68, <https://doi.org/10.1016/j.jmbbm.2014.05.002>.
- [50] J. Kadhkodapour, H. Montazerian, A.C. Darabi, A. Zargarian, S. Schmauder, The relationships between deformation mechanisms and mechanical properties of additively manufactured porous biomaterials, *J. Mech. Behav. Biomed. Mater.* 70 (2017) 28–42, <https://doi.org/10.1016/j.jmbbm.2016.09.018>.
- [51] C. Yan, L. Hao, A. Hussein, P. Young, Ti-6Al-4V triply periodic minimal surface structures for bone implants fabricated via selective laser melting, *J. Mech. Behav. Biomed. Mater.* 51 (2015) 61–73, <https://doi.org/10.1016/j.jmbbm.2015.06.024>.
- [52] A.A.A. Zadpoor, Mechanics of Additively Manufactured Biomaterials, Elsevier Ltd, 2017, <https://doi.org/10.1016/j.jmbbm.2017.03.018>.
- [53] E. Sallica-Leva, A.L. Jardini, J.B. Fogagnolo, Microstructure and mechanical behavior of porous Ti-6Al-4V parts obtained by selective laser melting, *J. Mech. Behav. Biomed. Mater.* 26 (2013) 98–108, <https://doi.org/10.1016/j.jmbbm.2013.05.011>.
- [54] S.L. Sing, J. An, W.Y. Yeong, F.E. Wiria, Laser and electron-beam powder-bed additive manufacturing of metallic implants: a review on processes, materials and designs, *J. Orthop. Res.* 34 (2016) 369–385, <https://doi.org/10.1002/jor.23075>.
- [55] A. Yu, C. Zhang, W. Xu, Y. Zhang, S. Tian, B. Liu, J. Zhang, A. He, B. Su, X. Lu, Additive manufacturing of multi-morphology graded titanium scaffolds for bone implant applications, *J. Mater. Sci. Technol.* 139 (2023) 47–58, <https://doi.org/10.1016/j.jmst.2022.07.035>.
- [56] A. Arjunan, M. Demetriou, A. Baroutaji, C. Wang, Mechanical performance of highly permeable laser melted Ti6Al4V bone scaffolds, *J. Mech. Behav. Biomed. Mater.* 102 (2020), 103517, <https://doi.org/10.1016/j.jmbbm.2019.103517>.
- [57] A. Arjunan, A. Baroutaji, A.S. Praveen, J. Robinson, C. Wang, Classification of biomaterial functionality, in: *Ref. Modul. Mater. Sci. Mater. Eng., Elsevier*, 2020, <https://doi.org/10.1016/B978-0-12-815732-9.00027-9>.
- [58] J. Parthasarathy, 3D modeling, custom implants and its future perspectives in craniofacial surgery, *Ann. Maxillofac. Surg.* 4 (2014) 9–18, <https://doi.org/10.4103/2231-0746.133065>.
- [59] L. Bai, C. Gong, X. Chen, Y. Sun, J. Zhang, L. Cai, S. Zhu, S.Q. Xie, Additive manufacturing of customized metallic orthopedic implants: materials, structures, and surface modifications, *Metals* 9 (2019), <https://doi.org/10.3390/met9091004>.
- [60] A. Nazir, O. Gokcekaya, K. Md Masum Billah, O. Ertugrul, J. Jiang, J. Sun, S. Hussain, Multi-material additive manufacturing: a systematic review of design, properties, applications, challenges, and 3D printing of materials and cellular metamaterials, *Mater. Des.* 226 (2023), 111661, <https://doi.org/10.1016/j.matdes.2023.111661>.
- [61] D. Melancon, Z.S. Bagheri, R.B. Johnston, L. Liu, M. Tanzer, D. Pasini, Mechanical characterization of structurally porous biomaterials built via additive manufacturing: experiments, predictive models, and design maps for load-bearing bone replacement implants, *Acta Biomater.* 63 (2017) 350–368, <https://doi.org/10.1016/j.actbio.2017.09.013>.
- [62] X.Y. Zhang, G. Fang, S. Leeftang, A.A. Zadpoor, J. Zhou, Topological design, permeability and mechanical behavior of additively manufactured functionally graded porous metallic biomaterials, *Acta Biomater.* 84 (2019) 437–452, <https://doi.org/10.1016/j.actbio.2018.12.013>.
- [63] R. Hedayati, S. Janbaz, M. Sadighi, M. Mohammadi-Aghdam, A.A. Zadpoor, How does tissue regeneration influence the mechanical behavior of additively manufactured porous biomaterials? *J. Mech. Behav. Biomed. Mater.* 65 (2017) 831–841, <https://doi.org/10.1016/j.jmbbm.2016.10.003>.
- [64] S. Bashir, R. Fitaihi, H.E. Abdelhakim, Advances in formulation and manufacturing strategies for the delivery of therapeutic proteins and peptides in orally disintegrating dosage forms, *Eur. J. Pharmaceut. Sci.* 182 (2023), 106374, <https://doi.org/10.1016/j.ejps.2023.106374>.
- [65] A. Sola, A. Trinchi, A.J. Hill, Self-assembly meets additive manufacturing: bridging the gap between nanoscale arrangement of matter and macroscale

- fabrication, *Smart Mater. Manuf.* 1 (2023), 100013, <https://doi.org/10.1016/j.smmf.2022.100013>.
- [66] J. Robinson, A. Arjunan, M. Stanford, I. Lyall, C. Williams, Effect of silver addition in copper-silver alloys fabricated by laser powder bed fusion in situ alloying, *J. Alloys Compd.* 857 (2021), 157561, <https://doi.org/10.1016/j.jallcom.2020.157561>.
- [67] A. Benady, S.J. Meyer, E. Golden, S. Dadia, G. Katarivas Levy, Patient-specific Ti-6Al-4V lattice implants for critical-sized load-bearing bone defects reconstruction, *Mater. Des.* 226 (2023), 111605, <https://doi.org/10.1016/j.matdes.2023.111605>.
- [68] A.I. Mirulla, G.M.M. Muccioli, S. Fratini, S. Zaffagnini, T. Ingrassia, L. Bragonzoni, B. Innocenti, Analysis of different geometrical features to achieve close-to-bone stiffness material properties in medical device: a feasibility numerical study, *Comput. Methods Progr. Biomed.* 221 (2022), 106875, <https://doi.org/10.1016/j.cmpb.2022.106875>.
- [69] D.M. Prada, A.F. Galvis, J. Miller, J.M. Foster, C. Zavaglia, Multiscale stiffness characterisation of both healthy and osteoporotic bone tissue using subject-specific data, *J. Mech. Behav. Biomed. Mater.* 135 (2022), 105431, <https://doi.org/10.1016/j.jmbbm.2022.105431>.
- [70] A. Synek, L. Ortner, D.H. Pahr, Accuracy of osseointegrated screw-bone construct stiffness and peri-implant loading predicted by homogenized FE models relative to micro-FE models, *J. Mech. Behav. Biomed. Mater.* 140 (2023), 105740, <https://doi.org/10.1016/j.jmbbm.2023.105740>.
- [71] M. Meskinfam, Polymer scaffolds for bone regeneration, *Charact. Polym. Biomater.* (2017) 441–475, <https://doi.org/10.1016/B978-0-08-100737-2.00017-0>.
- [72] M. Alizadeh-Osgouei, Y. Li, A. Vahid, A. Ataee, C. Wen, High strength porous PLA gyroid scaffolds manufactured via fused deposition modeling for tissue-engineering applications, *Smart Mater. Med.* 2 (2021) 15–25, <https://doi.org/10.1016/j.smaim.2020.10.003>.
- [73] D.A. Shimko, V.F. Shimko, E.A. Sander, K.F. Dickson, E.A. Nauman, Effect of porosity on the fluid flow characteristics and mechanical properties of tantalum scaffolds, *J. Biomed. Mater. Res. Part B Appl. Biomater.* 73 (2005) 315–324, <https://doi.org/10.1002/jbm.b.30229>.
- [74] M. Kumar, V. Sharma, Additive manufacturing techniques for the fabrication of tissue engineering scaffolds: a review, *Rapid Prototyp. J.* 27 (2021) 1230–1272, <https://doi.org/10.1108/RPJ-01-2021-0011>.
- [75] R. Vasireddi, B. Basu, Conceptual design of three-dimensional scaffolds of powder-based materials for bone tissue engineering applications, *Rapid Prototyp. J.* 21 (2015) 716–724, <https://doi.org/10.1108/RPJ-12-2013-0123>.
- [76] M. Kumar, S.S. Mohol, V. Sharma, A computational approach from design to degradation of additively manufactured scaffold for bone tissue engineering application, *Rapid Prototyp. J.* 28 (2022) 1956–1967, <https://doi.org/10.1108/RPJ-12-2021-0336>.
- [77] J. Li, Z. Xu, Q. Wang, G. Hu, Y. Wang, Coupling control of pore size and spatial distribution in bone scaffolds based on a random strategy for additive manufacturing, *Rapid Prototyp. J.* 25 (2019) 1030–1044, <https://doi.org/10.1108/RPJ-12-2017-0254>.
- [78] E. Dogan, A. Bhusal, B. Cecen, A.K. Miri, 3D Printing metamaterials towards tissue engineering, *Appl. Mater. Today* 20 (2020), 100752, <https://doi.org/10.1016/j.apmt.2020.100752>.
- [79] A. Arjunan, M. Singh, A. Baroutaji, C. Wang, Additively manufactured AlSi10Mg inherently stable thin and thick-walled lattice with negative Poisson's ratio, *Compos. Struct.* 247 (2020), 112469, <https://doi.org/10.1016/j.compstruct.2020.112469>.
- [80] A. Arjunan, S. Zahid, A. Baroutaji, J. Robinson, 3D printed auxetic nasopharyngeal swabs for COVID-19 sample collection, *J. Mech. Behav. Biomed. Mater.* (2020), 104175, <https://doi.org/10.1016/j.jmbbm.2020.104175>.
- [81] H. Cho, D. Seo, D.-N. Kim, Mechanics of auxetic materials, in: S. Schmauder, C.-S. Chen, K.K. Chawla, N. Chawla, W. Chen, Y. Kagawa (Eds.), *Handb. Mech. Mater.*, Springer Singapore, Singapore, 2018, pp. 1–25, https://doi.org/10.1007/978-981-10-6855-3_25-1.
- [82] H.M.A. Kolken, K. Lietaert, T. van der Sloten, B. Pournan, A. Meynen, G. Van Loock, H. Weinans, L. Scheys, A.A. Zadpoor, Mechanical performance of auxetic meta-biomaterials, *J. Mech. Behav. Biomed. Mater.* 104 (2020), <https://doi.org/10.1016/j.jmbbm.2020.103658>.
- [83] E.H. Schemitsch, Size matters: defining critical in bone defect size, *J. Orthop. Trauma* 31 (2017), <https://doi.org/10.1097/BOT.0000000000000978>. S20–S22.
- [84] D.N. Utomo, K.D. Hernugrahanto, M. Edward, L. Widhiyanto, F. Mahyudin, Combination of bone marrow aspirate, cancellous bone allograft, and platelet-rich plasma as an alternative solution to critical-sized diaphyseal bone defect: a case series, *Int. J. Surg. Case Rep.* 58 (2019) 178–185, <https://doi.org/10.1016/j.ijscr.2019.04.028>.
- [85] C. Christou, R.A. Oliver, M.H. Pelletier, W.R. Walsh, Ovine model for critical-size tibial segmental defects, *Comp. Med.* 64 (2014) 377–385. <https://www.ncbi.nlm.nih.gov/pubmed/25402178>.
- [86] A. Arjunan, J. Robinson, A. Baroutaji, A. Tuñón-Molina, M. Martí, Á. Serrano-Aroca, 3D printed cobalt-chromium-molybdenum porous superalloy with superior antiviral activity, *Int. J. Mol. Sci.* 22 (2021), <https://doi.org/10.3390/ijms222312721>.
- [87] J. Robinson, A. Arjunan, A. Baroutaji, M. Martí, A. Tuñón Molina, Á. Serrano-Aroca, A. Pollard, Additive manufacturing of anti-SARS-CoV-2 Copper-Tungsten-Silver alloy, *Rapid Prototyp. J.* (2021), <https://doi.org/10.1108/RPJ-06-2021-0131> ahead-of.
- [88] R.V. Lenth, Response-surface methods in R, using RSM, *J. Stat. Software* 32 (2009) 1–17, <https://doi.org/10.18637/jss.v032.i07>.
- [89] R.L. Lorza, M.Á.M. Calvo, C.B. Labari, P.J.R. Fuente, Using the multi-response method with desirability functions to optimize the Zinc electroplating of steel screws, *Metals* 8 (2018) 1–20, <https://doi.org/10.3390/met8090711>.
- [90] P. Cortez, Multi-Objective Optimization, 2014, pp. 99–117, https://doi.org/10.1007/978-3-319-08263-9_6.
- [91] S. Nayak, C. Tammer, P. Weidner, Multiobjective optimization, *Fundam. Optim. Tech. with Algorithms* (2020) 285–354, https://doi.org/10.1007/978-3-030-44723-6_7.
- [92] A. Ning, J.R.R.A. Martins, *Engineering Design Optimization*, 2020.
- [93] M.N. Oza, D.S. Shah, Theoretical and experimental modal analysis of centrifugal pump radial flow impeller, *IOP Conf. Ser. Mater. Sci. Eng.* 992 (2020), <https://doi.org/10.1088/1757-899X/992/1/012003>.
- [94] K.L. Gowtham, S.R. Srivatsa, Study of convergence of results in finite element analysis of a plane stress bracket, *J. Eng. Res. Appl.* (2018) 7–12.
- [95] E.M. Alawadhi, Meshing guide, *Finite Elem. Simulations Using ANSYS* 15317 (2020) 407–424, <https://doi.org/10.1201/b18949-12>.
- [96] N.S. Ghokale, *Practical Finite Element Analysis, Finite to Infinite*, Pune, India, 2008.
- [97] INTERNATIONAL STANDARD Verification of Static Uniaxial Testing — Calibration and Verification of the, 2018, p. 2018.
- [98] Y. Kang, J. Chang, Channels in a porous scaffold: a new player for vascularization, *Regen. Méd.* 13 (2018) 705–715, <https://doi.org/10.2217/rme-2018-0022>.
- [99] A. Bordin, A. Ghiotti, S. Bruschi, L. Facchini, F. Buccicotti, Machinability characteristics of wrought and EBM CoCrMo alloys, *Procedia CIRP* 14 (2014) 89–94, <https://doi.org/10.1016/j.procir.2014.03.082>.
- [100] S.R. Mohamed, S.A.C. Ghani, W. Sawangsrri, Mechanical properties of additive manufactured cocrmo meta-biomaterials for load bearing implants, *J. Tribol.* 21 (2019) 93–107.
- [101] K. Bari, A. Arjunan, Extra low interstitial titanium based fully porous morphological bone scaffolds manufactured using selective laser melting, *J. Mech. Behav. Biomed. Mater.* 95 (2019) 1–12, <https://doi.org/10.1016/j.jmbbm.2019.03.025>.
- [102] A. Ahmed, A. Majeed, Z. Atta, G. Guozhu, Dimensional quality and distortion analysis of thin-walled alloy parts of AlSi10Mg manufactured by selective laser melting, *J. Manuf. Mater. Process.* 3 (2019) 51, <https://doi.org/10.3390/jmmp3020051>.
- [103] J.H. Tan, W.L.E. Wong, K.W. Dalgarno, An overview of powder granulometry on feedstock and part performance in the selective laser melting process, *Addit. Manuf.* 18 (2017) 228–255, <https://doi.org/10.1016/j.addma.2017.10.011>.
- [104] V. Weibmann, P. Drescher, R. Bader, H. Seitz, H. Hansmann, N. Laufer, Comparison of single Ti 6 Al 4 V struts made using selective laser melting and electron beam melting subject to Part Orientation, *Metals* (2017), <https://doi.org/10.3390/met7030091>.
- [105] M. Benedetti, J. Klarin, F. Johansson, V. Fontanari, V. Luchin, G. Zappini, A. Molinari, Study of the compression behaviour of Ti6Al4V trabecular structures produced by additive laser manufacturing, *Materials* 12 (2019), <https://doi.org/10.3390/ma12091471>.
- [106] K.B. Hazlehurst, *The Adoption of Laser Melting Technology for the Manufacture of Functionally Graded Cobalt Chrome Alloy Femoral Stems*, 2014.
- [107] S.L. Sing, W.Y. Yeong, F.E. Wiria, B.Y. Tay, Characterization of titanium lattice structures fabricated by selective laser melting using an adapted compressive test method, *Exp. Mech.* 56 (2016) 735–748, <https://doi.org/10.1007/s11340-015-0117-y>.
- [108] M. De Wild, R. Schumacher, K. Mayer, E. Schkommodau, D. Thoma, M. Bredell, A. Kruse Gujer, K.W.K.W. Grätz, F.E.F.E. Weber, Bone regeneration by the osteoconductivity of porous titanium implants manufactured by selective laser melting: a histological and micro computed tomography study in the rabbit, *Tissue Eng.* 19 (2013) 2645–2654, <https://doi.org/10.1089/ten.tea.2012.0753>.
- [109] M. Speirs, B. Van Hooreweder, J. Van Humbeeck, J.-P.P. Kruth, Fatigue behaviour of NiTi shape memory alloy scaffolds produced by SLM, a unit cell design comparison, *J. Mech. Behav. Biomed. Mater.* 70 (2017) 53–59, <https://doi.org/10.1016/j.jmbbm.2017.01.016>.
- [110] L. Wang, J. Kang, C. Sun, D. Li, Y. Cao, Z. Jin, Mapping porous microstructures to yield desired mechanical properties for application in 3D printed bone scaffolds and orthopaedic implants, *Mater. Des.* 133 (2017) 62–68, <https://doi.org/10.1016/j.matdes.2017.07.021>.
- [111] N. Taniguchi, S. Fujibayashi, M. Takemoto, K. Sasaki, B. Otsuki, T. Nakamura, T. Matsushita, T. Kokubo, S. Matsuda, Effect of pore size on bone ingrowth into porous titanium implants fabricated by additive manufacturing: an in vivo experiment, *Mater. Sci. Eng., C* 59 (2016) 690–701, <https://doi.org/10.1016/j.msec.2015.10.069>.
- [112] S. Chowdhury, N. Yadaiah, C. Prakash, S. Ramakrishna, S. Dixit, L.R. Gupta, D. Buddhi, Laser powder bed fusion: a state-of-the-art review of the technology, materials, properties & defects, and numerical modelling, *J. Mater. Res. Technol.* 20 (2022) 2109–2172, <https://doi.org/10.1016/j.jmrt.2022.07.121>.
- [113] C. Du, Y. Zhao, J. Jiang, Q. Wang, H. Wang, N. Li, J. Sun, Pore defects in laser powder bed fusion: formation mechanism, control method, and perspectives, *J. Alloys Compd.* 944 (2023), 169215, <https://doi.org/10.1016/j.jallcom.2023.169215>.
- [114] L.C.B. Carolo, R.E. Cooper O, A review on the influence of process variables on the surface roughness of Ti-6Al-4V by electron beam powder bed fusion, *Addit. Manuf.* 59 (2022), 103103, <https://doi.org/10.1016/j.addma.2022.103103>.
- [115] J. Favre, P. Lohmuller, B. Piotrowski, S. Kenzari, P. Laheurte, F. Meraghni, A continuous crystallographic approach to generate cubic lattices and its effect on relative stiffness of architected materials, *Addit. Manuf.* 21 (2018) 359–368, <https://doi.org/10.1016/j.addma.2018.02.020>.

- [116] L.D. Bobbio, S. Qin, A. Dunbar, P. Michaleris, A.M. Beese, Characterization of the strength of support structures used in powder bed fusion additive manufacturing of Ti-6Al-4V, *Addit. Manuf.* 14 (2017) 60–68, <https://doi.org/10.1016/j.ADDMA.2017.01.002>.
- [117] G. Savio, S. Rosso, A. Curtarello, R. Meneghello, G. Concheri, Implications of modeling approaches on the fatigue behavior of cellular solids, *Addit. Manuf.* 25 (2019) 50–58, <https://doi.org/10.1016/j.addma.2018.10.047>.
- [118] A. Rodriguez-Contreras, M. Punset, J.A. Calero, F.J. Gil, E. Ruperez, J.M. Manero, Powder metallurgy with space holder for porous titanium implants: a review, *J. Mater. Sci. Technol.* 76 (2021) 129–149, <https://doi.org/10.1016/j.jmst.2020.11.005>.
- [119] H. Qu, Y. Peng, J. Huang, Z. Pan, F. Zhou, Modelling of the impact of stress concentration on permeability in porous medium based on machine learning method, *Geoenergy Sci. Eng.* 224 (2023), 211655, <https://doi.org/10.1016/j.geoen.2023.211655>.
- [120] L. Stohle, S. Wold, Analysis of variance (ANOVA), *Chemometr. Intell. Lab. Syst.* 6 (1989) 259–272, [https://doi.org/10.1016/0169-7439\(89\)80095-4](https://doi.org/10.1016/0169-7439(89)80095-4).
- [121] K. Molugaram, G.S. Rao, in: K. Molugaram, G.S.B.T. S.T, T.E. Rao (Eds.), Chapter 11 - ANOVA (Analysis of Variance), Butterworth-Heinemann, 2017, pp. 451–462, <https://doi.org/10.1016/B978-0-12-811555-8.00011-8>.
- [122] F. Rossi, V. Mirtchev, Chapter 4 - analysis of variance (ANOVA), in: F. Rossi, V. Mirtchev (Eds.), *Stat. Food Sci.*, Academic Press, San Diego, 2016, pp. 19–29, <https://doi.org/10.1016/B978-0-12-417179-4.00004-4>.
- [123] Z. Wang, L. Han, Y. Zhou, J. Cai, S. Sun, J. Ma, W. Wang, X. Li, L. Ma, The combination of a 3D-Printed porous Ti-6Al-4V alloy scaffold and stem cell sheet technology for the construction of biomimetic engineered bone at an ectopic site, *Mater. Today Bio.* 16 (2022), 100433, <https://doi.org/10.1016/j.mtbio.2022.100433>.
- [124] S. Mohandesnezhad, M.H. Monfared, S. Samani, A. Farzin, S.A. Poursamar, J. Ai, S. Ebrahimi-barough, M. Azami, 3D-printed bioactive Chitosan/Alginate/Hardystonite scaffold for bone tissue engineering: synthesis and characterization, *J. Non-Cryst. Solids* 609 (2023), 122261, <https://doi.org/10.1016/j.jnoncrsol.2023.122261>.
- [125] K. Dai, Z. Yang, L. Ding, Z. Yang, F. Hang, X. Cao, D. Chen, F. Zhao, X. Chen, 3D-printed strontium-doped BG-CaSiO₃-HA composite scaffolds promote critical bone defect repair by improving mechanical strength and increasing osteogenic activity, *Ceram. Int.* (2023), <https://doi.org/10.1016/j.ceramint.2023.03.095>.
- [126] A.H. Foroughi, C. Valeri, D. Jiang, F. Ning, M. Razavi, M.J. Razavi, Understanding compressive viscoelastic properties of additively manufactured PLA for bone-mimetic scaffold design, *Med. Eng. Phys.* (2023), 103972, <https://doi.org/10.1016/j.medengphy.2023.103972>.
- [127] J.M. Shum, B.C. Gadowski, S.J. Tredinnick, W. Fok, J. Fernandez, B. Nelson, R. H. Palmer, K.C. McGilvray, G.J. Hooper, C. Puttlitz, J. Easley, T.B.F. Woodfield, Enhanced bone formation in locally-optimised, low-stiffness additive manufactured titanium implants: an in silico and in vivo tibial advancement study, *Acta Biomater.* 156 (2023) 202–213, <https://doi.org/10.1016/j.actbio.2022.04.006>.
- [128] C. Song, L. Liu, Z. Deng, H. Lei, F. Yuan, Y. Yang, Y. Li, Jiakuo Yu, Research progress on the design and performance of porous titanium alloy bone implants, *J. Mater. Res. Technol.* 23 (2023) 2626–2641, <https://doi.org/10.1016/j.jmrt.2023.01.155>.
- [129] S.A. Che Ghani, S.R. Mohamed, M. Sha'ban, W.S. Wan Harun, N.A.Z. Md Noar, Experimental investigation of biological and mechanical properties of CoCrMo based selective laser melted metamaterials for bone implant manufacturing, *Procedia CIRP* 89 (2020) 79–91, <https://doi.org/10.1016/j.procir.2020.05.122>.